GEORG-AUGUST-UNIVERSITÄT GÖTTINGEN

Fakultät für Physik

Bachelor's Thesis

Studien zur zeitgenauen Ladungsmessung mit dem Auslesechip der ersten Stufe des Ausbaus des ATLAS Pixeldetektors

Studies of in-time charge measurement with the read-out chip of the first upgrade stage of the ATLAS Pixel Detector

prepared by

Mattia Donzelli

at the II. Institute of Physics

Thesis period:	7th November 2011 until 13th February 2012
First referee:	PD. Dr. Jörn Große-Knetter
Second referee:	Prof. Dr. Arnulf Quadt
Publication number:	II.Physik-UniGö-BSc-2012/01

Abstract

This thesis presents a study on the new FE-I4 read-out chip of the ATLAS Pixel Detector. The first sections describe the functionality of semiconductor detectors in general and of the ATLAS Pixel Detector in particular. For the acquisition of data, the USBpix test system was utilized. The analysis consists of two parts. The first refers to the tuning of the analogue amplification part and the digitization process on the chip in order to obtain a homogeneous response. A proposal for an automated tuning strategy that determines the optimal configuration of the chip parameters *PrmpVbpf* and *FdacVbn* was successfully developed and is presented here. The second part deals with time-walk effects and the determination of the in-time threshold. The accuracy of the preceding t_0-scan was increased by implementing an alternative linear fit routine for data sets that cannot be fitted with an S-curve.

Contents

1. Introduction

Particle physics examines the constituents of matter and how they interact in order to find the elementary particles which the world and the universe consist of. The standard model of particle physics describes leptons, quarks, the four gauge bosons and the Higgs-Boson. Except for the Higgs-Boson, all of the standard model particles have been detected in various high energy physics experiments.

The search for the Higgs-Boson is one of the main tasks of the LHC[1] at CERN[2]. The LHC is a synchrotron storage ring which is designed for the collision of two proton beams at a maximum centre of mass energy of 14 TeV [1]. It is situated in a 27 km long tunnel that was dug for LEP[3], the previous accelerator at CERN. In the coming years the design luminosity[4] of $1.0 \cdot 10^{34}\,\mathrm{cm}^{-2}\mathrm{s}^{-1}$ [1] is expected to be reached.

Another important task of the LHC is the search for new physics beyond the standard model. While most of the processes that occur on earth can be described by the standard model, astronomical observations suggest the existence of as yet unknown kinds of matter or interaction mechanisms. For hypothetic theories beyond the standard model the LHC may provide new results.

For the detection of the collision products there are several experiments installed at the collision points – among which A Large Ion Collider Experiment (ALICE), A Toroidal LHC ApparatuS (ATLAS), Compact Muon Solenoid (CMS) and Large Hadron Collider beauty (LHCb) are the best known.

The ATLAS Detector [2] is a nearly hermetic[5] general-purpose detector. It consists of different subsystems: the Inner Detector for high resolution tracking of charged particles, a calorimeter system to measure the particle's energy and muon chambers in the outermost layer for the detection of muons. The detector covers almost 4π of the solid angle around the interaction point in order to detect all particles produced in the collision, except for

[1] Large Hadron Collider
[2] Conseil Européen pour la Recherche Nucléaire
[3] Large Electron-Positron Collider
[4] The luminosity gives the number of expected events per time and scattering cross-section.
[5] Hermetic detectors cover the full solid angle

neutrinos, which have an interaction probability close to zero.
A magnetic field in the detector forces charged particles on a curved trajectory, which allows for the determination of their momentum. In order to obtain a good measurement of the curve radius, a high-resolution tool is required. The Inner Detector, which occupies a radius of 1.15 m at a length of 7 m around the interaction point, serves this purpose. It is composed of the Pixel Detector, which is the subject of this study, at the centre followed by the Semiconductor Tracker and the Transition Radiation Tracker at the outer regions. The ATLAS Pixel Detector consists of three layers of hybrid silicon detectors [3] at average radii of 50.5 mm, 88.5 mm and 122.5 mm in the detector barrel and 3 disks in the endcaps at a distance of 495 mm, 580 mm and 650 mm from the interaction point.
In order to compensate for the loss in efficiency due to radiation damage in the existing detector layers, an additional detector layer, the Insertable B-Layer (IBL) [4], will be added to the detector. The upgrade will be implemented during the next long shutdown period of the LHC in 2013. Situated close to a new beam pipe with a reduced diameter of 47 mm [5], the IBL is expected to increase the tracking resolution.
The research done for this thesis is focussed on the verification of the properties of the read-out electronics for the IBL. The first part refers to the digitization process of the incoming data. The aim is to develop an automated strategy for finding the optimal fine adjustment of the preamplifier feedback current. The second part deals with the timing of the read-out chip. The requirements for assigning an event in the detector to the right bunch crossing[6] are explained here as well as the criteria to distinguish between in-time hits and delayed hits.

[6]The collision of two proton bunches in the detector is called bunch crossing.

2. The ATLAS Detector

The ATLAS Detector [2] (Figure 2.1) is composed of five different parts, each having a special purpose in radiation detection: the Inner Detector, Electromagnetic Calorimeter, Hardronic Calorimeter, Muon Spectrometer and the Magnet System.
The last consists of a solenoid around the Inner Detector and three toroidal coil systems, two at the endcaps and one in the barrel of the detector. They provide a magnetic flux density of about 2 Tesla in the Inner Detector and reach a magnetic field of about 4 Tesla in the barrel and the endcaps. Due to this magnetic field, charged particles are forced on a curved trajectory, which allows the determination of the particles' momentum.
Calorimeters measure the radiation energy by generating particle showers. The distinction between electromagnetic and hadronic calorimeters is based on the main interaction mechanisms that induce the particle showers.
The Electromagnetic Calorimeter stops electrons and photons mainly by bremsstrahlung and pairproduction processes (see Chapter 3.1.1). Lead plates induce the particle showers, and liquid argon is used for the shower detection. Charged hadrons and muons leave a slight signal in the Electromagnetic Calorimeter, but in general they are not stopped.
In the Hadronic Calorimeter all kinds of hadrons shower. Iron is used as shower material whereas scintillators[1] form the active part for particle detection.
Muons are the only type of particles that leave a signal in the region outside the calorimeters. The Muon Spectrometer is a tracking system developed to measure the momentum of muons with a high resolution. The detection is done by gaseous detectors. The muon chambers specify the dimensions of the ATLAS Detector, which is 44 m long and 25 m in diameter.
In the central position lies the Inner Detector, which consists of three subsystems. The Semiconductor Tracker is a microstrip device with four detector layers at radii of about 30 cm, 37 cm, 45 cm and 52 cm and nine disks in each endcap.
The outermost part of the Inner Detector is the Transition Radiation Tracker, a gaseous

[1] A scintillator emits a light signal that can be detected using a photomultiplier whenever a fast charged particle passes through.

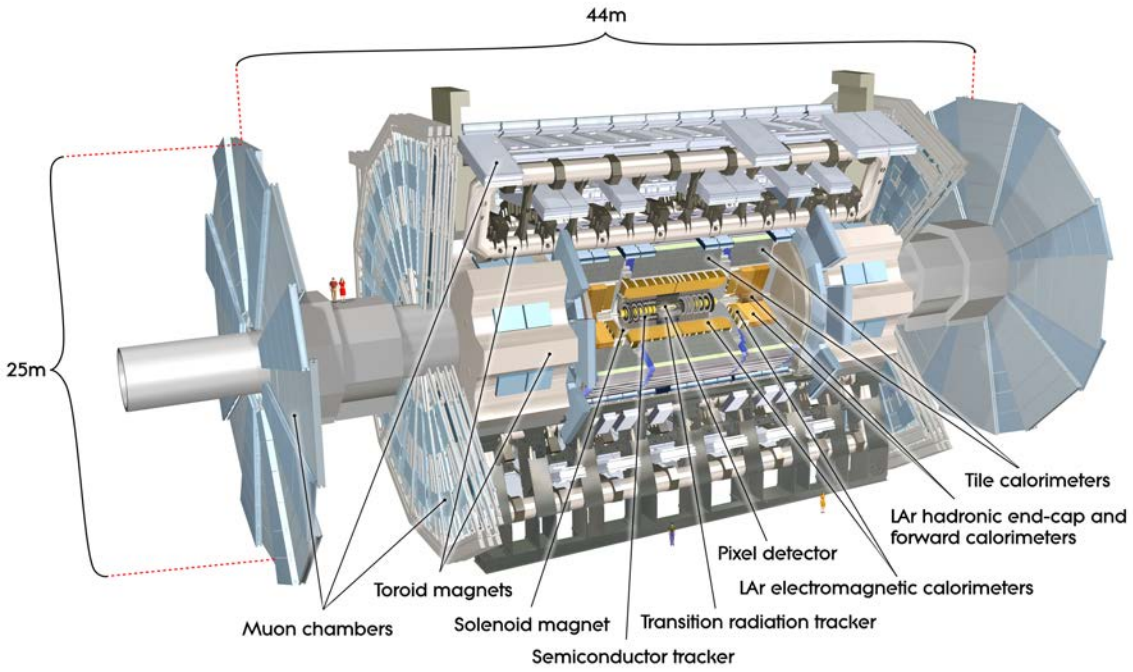

Figure 2.1.: Computer generated image of the ATLAS Detector [6].

detector providing particle tracking at low costs but also with a lower resolution compared to silicon detectors.
The innermost part of the detector is the Pixel Detector which is described in the following chapter.

3. The ATLAS Pixel Detector

The ATLAS Pixel Detector (Figure 3.1) is a hybrid semiconductor detector with silicon sensors (see Sections 3.1 and 3.2). It has a cylindrical configuration coaxial to the beam pipe. The barrel of the detector is built of three sensor layers at radii of 50.5 mm, 88.5 mm and 122.5 mm [7] from the beam axis with a length of 801 mm. In total, it consists of 1 456 modules[1], each with 46 080 pixels. The endcaps are made up of three disks at a distance of 495 mm, 580 mm and 650 mm from the interaction point. Each disk is composed of 48 modules of the same type as those situated in the barrel.

All in all, the ATLAS Pixel Detector has 1744 modules resulting in 80 363 520 read-out channels. It covers an active area of $1.73\,\mathrm{m}^2$ and it is able to detect particles up to a pseudorapidity[2] of $|\eta| < 2.5$.

The main task of the ATLAS Pixel Detector is the measurement of tracks of charged particles with the highest possible spatial resolution. Finely segmented pixel sensors allow for a precise reconstruction of vertices and a distinction between primary and secondary decays.

Most of the pixels have a size of $50\,\mu\mathrm{m} \times 400\,\mu\mathrm{m}$. In the region between the read-out chips of a module the pixels have a size of $50\,\mu\mathrm{m} \times 600\,\mu\mathrm{m}$.

To keep down influences on the particles trajectory due to multiple scattering (see Formula 3.5 in Chapter 3.1.1) the material budget is kept low.

The principles of semiconductor detectors and hybrid read-out technology are described in the following chapters.

[1] A module is made of a silicon sensor equipped with 16 front-end chips for read-out and a module control chip.

[2] The definition of the pseudorapidity is given by $\eta = -\ln\left[\tan\left(\frac{\theta}{2}\right)\right]$, where θ denominates the polar angle with the z-axis in beam direction.

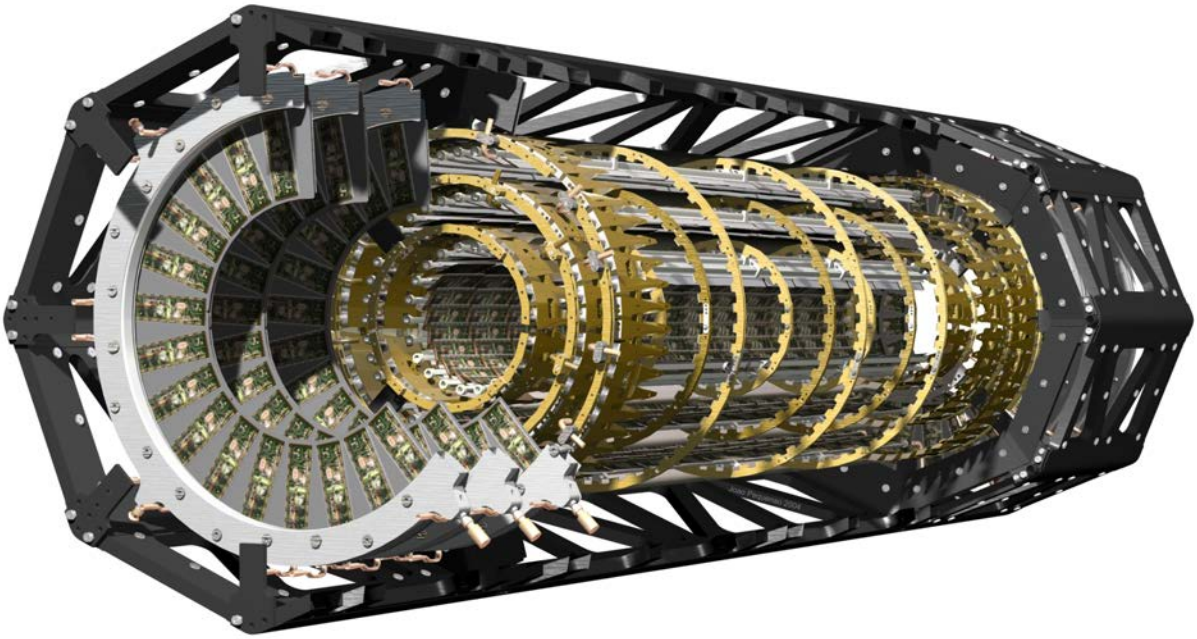

Figure 3.1.: Cutaway model of the ATLAS Pixel Detector [8].

3.1. Signal creation

3.1.1. Energy loss of charged particles in matter

A fast charged particle passing through matter interacts with its electrons. Thus the particle loses energy that is deposited in the interacting material. The medium amount of energy loss is described by the Bethe formula [9]:

$$-\left\langle \frac{\mathrm{d}E}{\mathrm{d}x} \right\rangle = Kz^2\rho\frac{Z}{A\beta^2}\left[\frac{1}{2}\ln\left(\frac{2m_\mathrm{e}\gamma^2v^2W_\mathrm{max}}{I^2}\right) - 2\beta^2 - \delta - 2\frac{C}{Z}\right], \tag{3.1}$$

with

$K = 2\pi N_\mathrm{A} {r_\mathrm{e}}^2 {m_\mathrm{e}}^2 c^2 = 0.1535\,\mathrm{MeV}c^2/\mathrm{g}$,
r_e the electron radius,
m_e the electron mass,
N_A the Avogadro constant,
I the average ionization potential,
Z the atomic number,
A the atomic mass number,

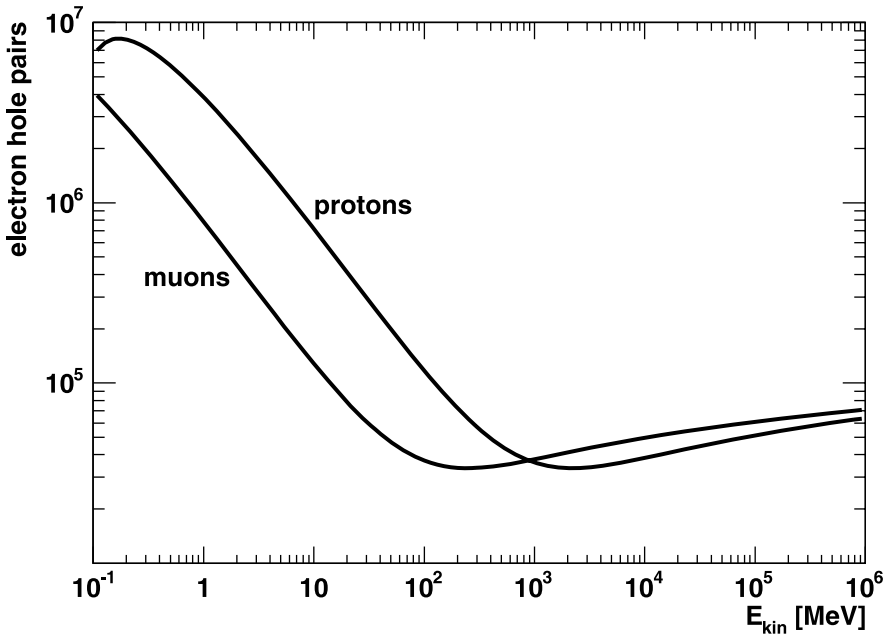

Figure 3.2.: Number of electron-hole pairs generated in a 300 μm thick silicon layer plotted versus energy [10].

ρ the mass density of the medium,
z the charge of the traversing particle,
v the velocity of the traversing particle,
$\beta = v/c$,
$\gamma = 1/\sqrt{1-\beta^2}$ the Lorentz factor,
δ a density correction and
C a shell correction.

Usually the medium energy loss is normalized to the mass density of the medium, the dimension of $-\left\langle \frac{dE}{dx} \right\rangle$ then becomes $\frac{\text{eV}}{\text{g/cm}^2}$. An example of the Bethe curve is shown in Figure 3.2. The maximum energy that can be transferred in a central impact is given by

$$W_{\max} = \frac{2m_e c^2 \beta^2 \gamma^2}{1 + \frac{2m_e}{M} \cdot \sqrt{1+\beta^2\gamma^2} + \left(\frac{m_e}{M}\right)^2}\,, \tag{3.2}$$

where M denominates the mass of the incident particle. The Bethe formula gives the medium deposition of energy which is subject to statistical fluctuations. The Landau distribution[3] describes the probability that a certain amount of energy in a thin layer of matter is deposited [11]. Since the distribution is not symmetric, the mean value is greater than

[3]The Landau distribution $p(x)$ is defined by $p(x) = \frac{1}{2\pi i}\int_{c-i\infty}^{c+i\infty} e^{s\log s + xs}\, ds$.

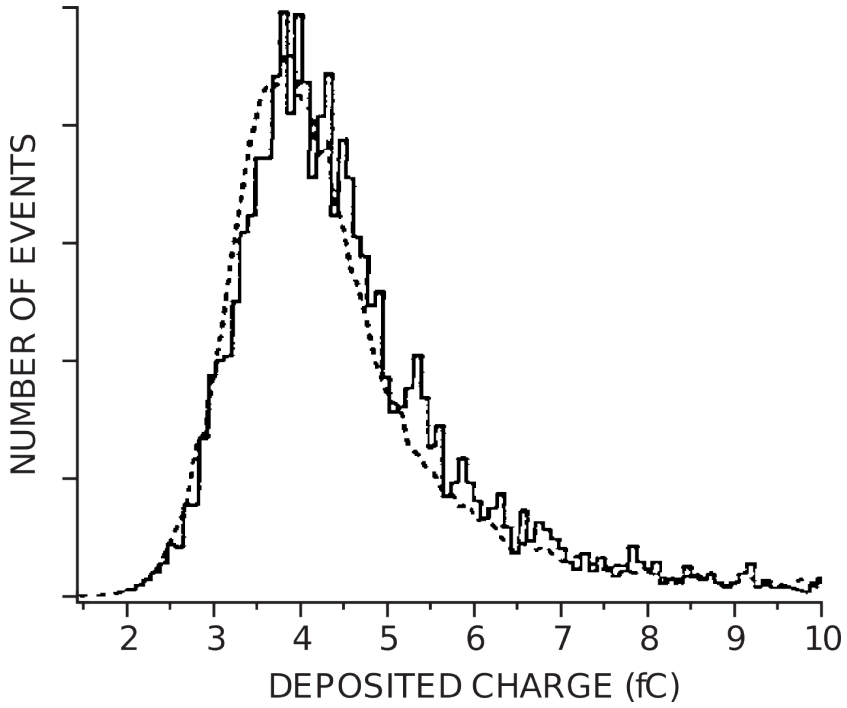

Figure 3.3.: Deposited charge of electrons with a momentum of $p = 1,5\,\mathrm{MeV/c}$ in a silicon detector in comparison to the Landau distribution (dashed line) [11].

the most probable value. In Figure 3.3 the theoretical Landau distribution is compared to experimental data.

A particle with $\beta\gamma \approx 3$ lies in the minimum of $\left\langle -\frac{\mathrm{d}E}{\mathrm{d}x} \right\rangle$ and is called minimum ionizing particle (MIP). As the curve of $-\left\langle \frac{\mathrm{d}E}{\mathrm{d}x} \right\rangle$ rises only slightly for $\beta\gamma > 3$ and in order to simplify matters, all particles with $\beta\gamma \geq 3$ can be considered to be MIPs.

The Bethe formula is valid for charged particles heavier than electrons. The dominating process of energy loss in matter regarding electrons is the production of bremsstrahlung in the electric field of an atomic nucleus. Electrons lose energy by emitting photons. If their energy is sufficiently high, these photons can produce electron-positron-pairs. The mean distance between the occurence of bremsstrahlung and pair production processes is the radiation length X_0. In an approximation the energy loss of an electron obeys the following law [12]:

$$-\left\langle \frac{\mathrm{d}E}{\mathrm{d}x} \right\rangle \simeq \frac{E}{X_0}\ [\mathrm{MeV/X_0}]\ . \tag{3.3}$$

The radiation length can be estimated by

$$X_0^{-1} = 32.2 \cdot 10^{-28} \cdot N_\mathrm{A} \rho \alpha \frac{Z(Z+1)}{A} \ln\left(\frac{183}{Z^{1/3}}\right) \tag{3.4}$$

and depends on the mass density ρ as well as on the atomic number Z, the atomic mass number A, the Avogadro constant N_A and the fine-structure constant $\alpha = 1/137$.
Due to Coulomb interactions with the atomic nuclei, the incident particles are deflected from their initial direction of motion. After traversing a thickness L of material, the root mean square deflection angle θ_rms – owing to multiple Coulomb scattering – is given by the Rossi-Greisen equation [12]:

$$\theta_\mathrm{rms} = \sqrt{\langle \theta^2 \rangle} = \sqrt{\frac{4\pi}{\alpha}} \frac{m_\mathrm{e} c^2 z}{vp} \sqrt{\frac{L}{X_0}} \,, \tag{3.5}$$

where v, p and z denominate the incident particle speed, momentum and charge in units of e.

3.1.2. Charge generation in semiconductor detectors

Semiconductors and doping

A semiconductor is a crystalline material that at standard conditions behaves like an insulator but under certain circumstances has conductor properties. These characteristics can be explained on the basis of the energy band model from solid-state physics. It assumes that the valence electrons[4] are on an energy level called the valence band, where they cannot move from one atom to another, whereas electrons in the more highly situated conduction band can move through the solid body. Energy areas that are not covered by existing energy bands are forbidden for electrons.
If the valence band and the conduction band share overlapping energy ranges, the electrons can switch from the valence band to the conduction band, and the solid body turns conductive. If there is an energy gap between valence band and conduction band, the electrons cannot switch to the conduction band, consequently the solid body is an insulator. Semiconductors have a small band gap (~1.1 eV for silicon) between valence band and conduction band. By supplying energy to the electrons (e.g. by heating the crystal) they can be excited to the conduction band leaving a mobile hole in the valence band.

[4] In the shell model of atomic physics the term valence electron denominates electrons on the highest level of potential energy in the ground state.

These free electrons and holes can recombine, which in turn results in a reduction of the semiconductor's conductivity and a finite lifetime of these charge carriers.
There are two reasons for the movement of free charge carriers. Diffusion leads to an undirected movement in order to equalize the distribution of charge carriers. Directed movements are induced by external electric fields that accelerate the charge carriers unless an equilibrium between the electric force and collisions with crystal constituents is reached.
The density of free charge carriers in a semiconductor can be increased by doping the crystal with a small fraction of atoms with three or five valence electrons. Usually a semiconductor has four valence electrons, thus a doped crystal has an overflow of or a lack of electrons compared to its typical structure. In case of n-type doping (n stands for the negative charge of the additional electrons) the residual electrons are in the valence band, rendering the crystal conductive. P-type (p stands for the positive charge of the missing electron) doped semiconductors show a not completely occupied valence band. As these holes in the valence band are mobile, they act as free charge carriers and give the semiconductor conductive characteristics.

The p-n-junction

A p-n-junction is an electronic component that conducts electric current in only one direction. It consists of two semiconductors, one p-type doped and the other n-type doped, that are directly connected to each other. The free charge carriers on both sides diffuse to the respective opposite side of the junction, where they mainly recombine with contrary charge carriers. This movement causes a counteracting electric field that comes to an equilibrium with the diffusion process. As a consequence, the area around the junction is nearly free of charge carriers.
Applying a positive voltage to the p-type side and a negative voltage to the n-type side forces the electrons and holes to move to the respective other side of the junction. In this constellation the p-n-junction functions as a conductor. If the polarity of the voltage supply is inverted, the free charge carriers are forced to move to the ends of the semiconductor, resulting in an expansion of the area free of charge carriers around the junction. At a sufficiently high voltage the semiconductor is completely depleted. In the depletion mode only a small leakage current flows through the p-n-juncion.

Moving charge and the Ramo theorem

If a charged particle penetrates a semiconductor, the deposited energy – according to the Bethe formula – enables valence electrons to switch to the conduction band. But compared to the number of charge carriers originating from doping and thermal excitation, the amount of newly generated charge carriers is slight and their lifetime is small due to recombination. Thus, for the detection of charged particles completely depleted semiconductors are used. Here, the generated charge carriers do not recombine and thus they are well detectable. The field that depletes the semiconductor also accelerates the generated charge carriers to the electrodes where they can be detected.
Such a semiconductor, surrounded by two metal contacts, can be considered as a capacitor, charged by the external bias voltage. The generated charge should be detectable as soon as it reaches the metal contacts. The drift velocity $v_{e/h}$ of the electrons and holes is given by

$$v_{e/h} = \mu_{e/h} \frac{V_b}{d}, \qquad \mu_e >> \mu_h \tag{3.6}$$

with V_b the bias voltage and d the thickness of the diode. The mobility μ is much greater for electrons than for holes, thus in general the electrons reach the electrode earlier than the holes.
But according to Ramo's theorem [11] a signal is detectable before the charge reaches the electrodes. Since moving electric charges cause a varying density of electrical flux on the electrodes, the charge induced on the electrodes is not constant in time and an electrical current is created. The time integral of this current is equal to the overall charge generated in the sensor and in the end leads to the same result as the classical assumption on a capacitor.

3.1.3. Radiation damage

Radiation damage does not only act on the electrons of the sensor material but also on the atomic nuclei, changing the properties of the atomic lattice of the semiconductor [9]. Different types of defects cause a loss in quality of the semiconductor. Most of the defects are not permanent. Interstitials and vacancies in the atomic lattice are mobile and can recombine.
The most common effects of radiation damage are generation-recombination centres, trap-

ping centres, and the type-inversion. In generation-recombination centres, an elevated rate of electron-hole pair generation and annihilation exists. They reduce the mean life time of free charge carriers and increase the leakage current in depletion mode. Both effects reduce the quality of the signal obtained from the sensor and lead to an increased noise level.
Trapping centres stop charge carriers and release them with a delay (which is usually much longer than the drift time to the end of the sensor), thereby decreasing the signal according to RAMO's theorem.
The type inversion describes the generation of electron acceptors in the semiconductor. Thus the effective doping concentration of an originally n-type semiconductor can switch to p-type. As a consequence the voltage needed for a full depletion increases. When the depletion voltage reaches the breakdown voltage, the sensor cannot be completely depleted anymore, thus the depletion zone disposable for the particle detection and also the obtained signal decrease.

3.2. Hybrid detectors

Modern semiconductor pixel detectors are so-called hybrid detectors [9, 10]. They include a sensor for the charge generation and separate read-out electronics. The semiconductor sensor can be segmented in pixels of a size down to $\sim 50\,\mu\text{m} \times 50\,\mu\text{m}$, the thickness is in the order of $250\,\mu\text{m}$.
The read-out electronics are located in a front-end chip (FE) that is segmented in the same way as the sensor. Every pixel of the front-end chip provides the same electronics, in general signal amplification, noise discrimination, digitization and buffering for a later read-out.
To get a hybrid module, the sensor and the front-end chip are connected via bump-bonding. Small solder bumps provide the connection between the sensor pixel and the contact area on the front-end chip. The depletion voltage is applied on the non-segmented backplane of the sensor, so that the side of the front-end chip is grounded.
If the sensor is larger than the front-end chip, it can be equipped with multiple front-end chips. In this case, usually an additional module control chip (MCC) is added to the configuration that handles the communication to and from the FE. The configuration of the FE and the trigger[5] distribution is done by the MCC as well as the read-out of the

[5] A trigger decides on a small set of information whether an event is relevant or not and - if necessary - requests the read-out of further data.

requested data and a first processing.

3.3. The Insertable B-Layer

The ATLAS Detector is expected to collect about $300\,\mathrm{fb}^{-1}$ of data by 2018 [13]. The resulting radiation on the innermost detector parts will cause damages in the semiconductor structure that lead to a significant decrease of signal quality and finally to the failure of the detector. A replacement of damaged detector components is therefore necessary to keep up the detector tracking performance.
In 2013, the LHC will be shut down for maintenance and upgrade operations. During this period a new barrel layer of hybrid detector modules will be inserted into the ATLAS Pixel Detector. This "Insertable B-Layer" (IBL) [5] will be placed between a new beam pipe with a reduced diameter of 47 mm and the existing B-Layer at a radius of 50.5 mm. 14 arrays of 32 front-end chips each form a barrel of 643 mm length covering a pseudorapidity range up to $|\eta| < 3$. In functional interaction with the three existing Pixel Detector layers, the tracking and b-tagging efficiency will increase. The short distance of just 34 mm from the beam axis imposes high demands on the radiation hardness.
The IBL sensors are designed with a pixel size of $50\,\mu\mathrm{m} \times 250\,\mu\mathrm{m}$ and allow for a better resolution in z-direction than the current sensors.

3.3.1. The FE-I4 chip

With the reduced distance from the beam pipe and a luminosity that is expected to exceed[6] $2 \cdot 10^{34}\,\mathrm{cm}^{-2}\mathrm{s}^{-1}$ the current read-out chip front-end I3 (FE-I3) would not be able to process the expected hit rate. Therefore a new chip, the FE-I4 [14, 15] has been developed. It supports the parallel read-out of 80×336 pixels. The circuit diagram of the in-pixel electronics is shown in Figure 3.4.
The sensor is connected via bump bonding to the pad indicated as Q_{in}. A charge sensitive amplifier (*Preamp* and C_{fl}) creates an output voltage that is proportional to the collected charge and inversely proportional to the feedback capacitor C_{fl} [11]. After amplifying the signal caused by a charged particle, the amplifier has to be reset by discharging the capacitor C_{fl} until the output voltage returns to zero. This is achieved by a constant feed-

[6] In the High Luminosity Large Hadron Collider (HL-LHC) upgrade after 2020 [4].

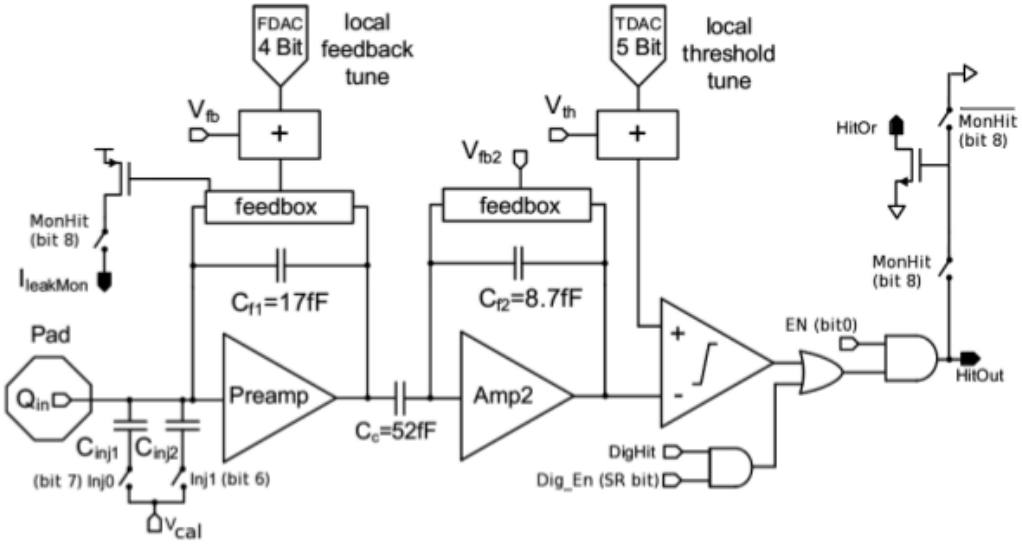

Figure 3.4.: Amplifier and discriminator circuit of the FE-I4 [14].

back current (*feedbox*). The first amplifier is followed by another one (*Amp2* and C_{f2}) and subsequently a discriminator for noise suppression fires whenever the amplified signal exceeds a predefined threshold. In Figure 3.5 the resulting signals are sketched.
The rise time that is necessary to charge the feedback capacitor C_{f1} is independent of the signal amplitude but significantly different from zero. This causes the triangle-shaped output signal. The pitch of the descending edge is constant and depends on the feedback current.
A specific characteristic of the FE-I4 is linked to the constant signal rise time. The "time-walk effect" is most notable at small amounts of charge. As Figure 3.5 shows, the discriminator's rising edge delays much more when small charges are received. If the charge is small compared to the threshold, the rising edge of the discriminator moves to the time window of the following bunch crossing. Consequently, these hits are allocated to the wrong event. The minimum charge that leads to a time-walk < 25 ns and therefore does not lead to misassignment is called "in-time threshold".
The digitization of charge information is done by utilizing the discriminator output signal. In a rough approximation (see Equation 5.1) the time span during which the discriminator is active is proportional to the charge collected in the detector. This time is called "time over threshold" (ToT) and is measured in units of 25 ns[7]. For a later read-out the digitized information is stored in a 4-bit word in a register together with the time at which the event

[7] 25 ns is the distance of two proton bunch crossings at the LHC, corresponding to a bunch crossing frequency of 40 MHz.

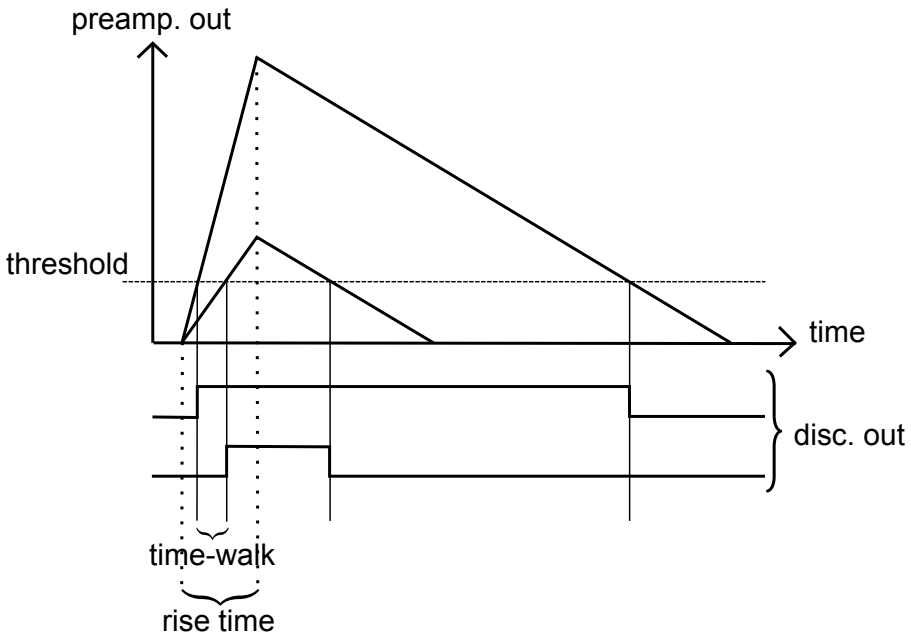

Figure 3.5.: The operating principle of the discriminator and the time-walk effect at different amounts of charge.

occurred. 14 of the 16 register values are used to encode the ToT. Hits that exceed a ToT of 13 are treated like hits with a ToT of 13. The two remaining values are reserved for special purposes. This data is only forwarded if requested by an external trigger, otherwise it is automatically deleted after a certain time has elapsed. This procedure reduces the amount of data processed and moved through the detector, therefore it leads to a lower power consumption and thus also to a lower cooling effort.

On the FE-I4 chip several features are implemented for tuning and adjustment of the chip behaviour. Functions like the discriminator threshold and the amplifier feedback current can be influenced by various parameters. The relevant parameters are explained in the following section.

For chip testing and calibration the FE-I4 provides two methods to introduce artificially generated signals in the amplification and digitization part of the electronics.

For testing of the digital part, a signal can be injected at the discriminator output in order to examine the digitization, the correct storage and read-out.

In order to test the analogue part, the capacitors C_{inj1} and C_{inj2} can be charged by the voltage V_{cal}. By closing the switches Inj0 and/or Inj1 (they can be activated independently) the capacitor discharges through the amplifier whose output is processed by the discriminator. Thus the signal is processed like a charge collected from a connected silicon sensor. The moment of injection is controlled by the "strobe" signal.

3.3.2. Important parameters and functions of the FE-I4

All parameters of the FE-I4 are regulated by DACs[8] of different bit-lengths.
As mentioned before, V_{cal} is the voltage applied to the capacitors for test charge injection. One digital step in the 10-bit register *PlsrDAC* results in an increase of V_{cal} of $\sim$1.5 mV, the exact value has to be measured with an external voltmeter. The test capacitors have the values $C_{\text{inj1}} = 1.9\,\text{fF}$ and $C_{\text{inj2}} = 3.9\,\text{fF}$. If used together, due to the capacitance of the conducting tracks, the capacitance is not equal to the sum of C_{inj1} and C_{inj2}: C_{inj1} & $C_{\text{inj2}} = 5.7\,\text{fF}$.
The discriminator threshold can be modified by three different parameters, *Vthin_AltCoarse*, *Vthin_AltFine* and *TDAC*. The first two of these set the global threshold for all pixels. *TDAC* is a 5-bit in-pixel correction for the fine tuning of the threshold. In-pixel means that the value can be set for every pixel individually. This correction is necessary because of the inhomogeneous chip characteristics resulting from fabrication fluctuations.
Three different parameters control the preamplifier feedback current. *PrmpVbpf* (8-bit) sets the global feedback current, while *FDAC* (4-bit) is for the in-pixel fine tuning. Additionally the parameter *FdacVbn* (8-bit) varies the step size of the *FDAC* correction.

[8] Digital-to-analogue converter

4. The measurement setup

4.1. The USBpix test system

The USBpix test system [16] is a compact USB-based test system. It supports testing of FE-I3 and FE-I4 read-out chips. Both hardware and software are designed modularly. A schematic sketch of the test system is shown in Figure 4.1. The hardware used is depicted in Figure 4.2. It is composed of a Multi-IO board, an adapter card and a single chip support card.

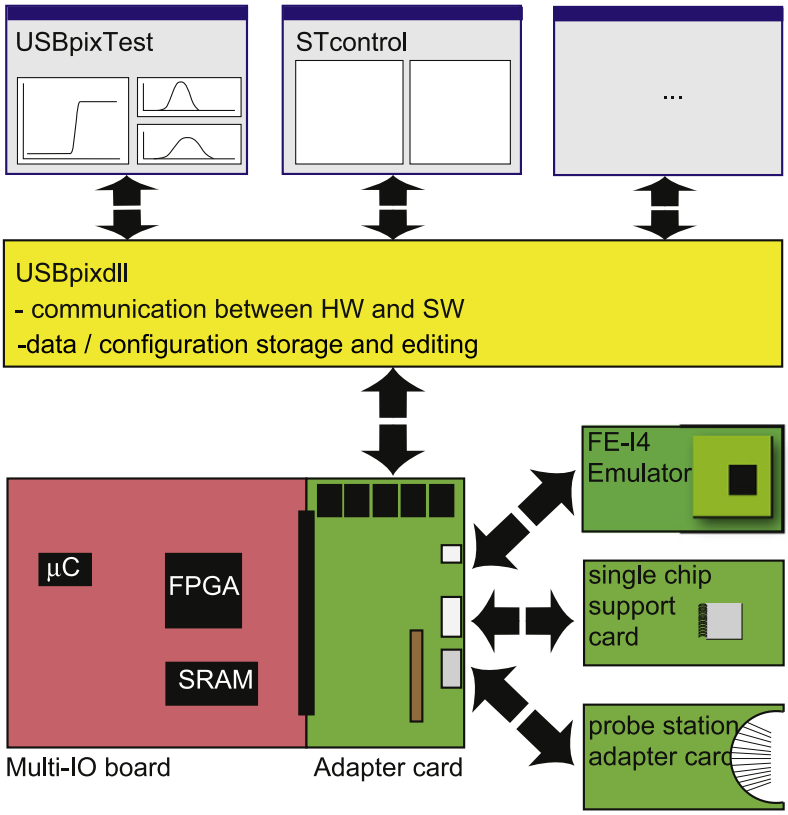

Figure 4.1.: Schematic overview of the USBpix hardware and software [16].

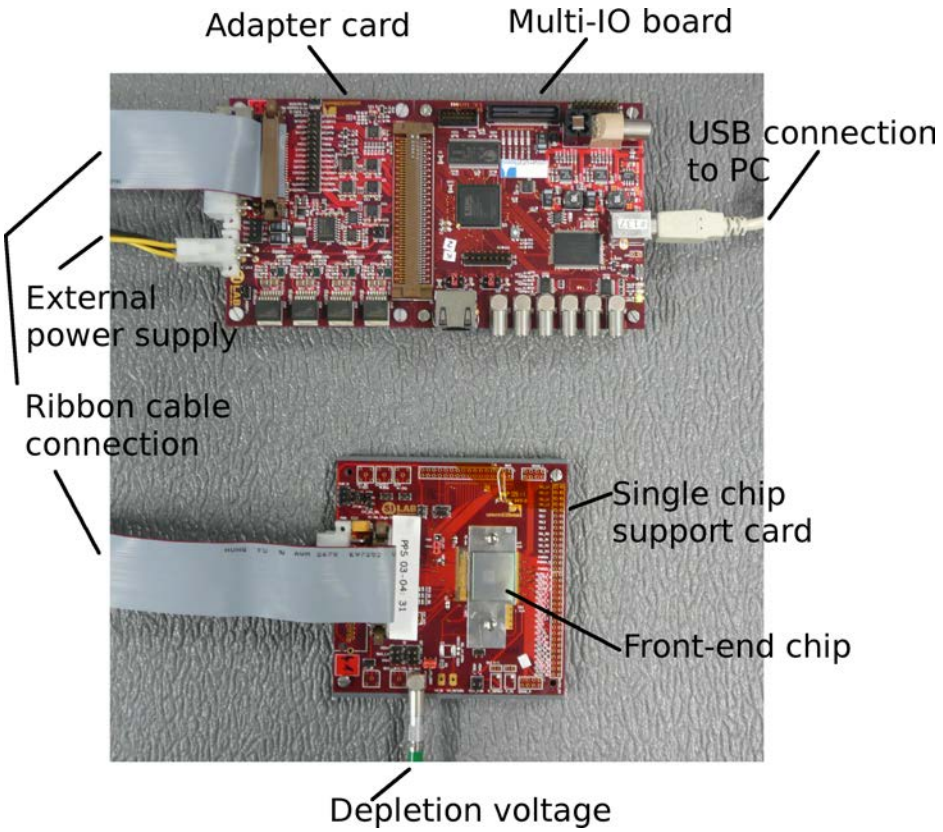

Figure 4.2.: The utilized hardware.

The Multi-IO board provides a USB micro controller and an FPGA[1] that histograms data and stores it in an SRAM[2]. The scan routines are controlled by the USB micro controller. Therefore, the communication to the PC during the scan is kept low and the scan time is abbreviated.
The Multi-IO board is connected to an adapter card which converts the signal via LVDS[3] transmitters or CMOS[4] level shifters to a 50 pin connector together with the power supply. An incoming voltage of 2.0 V is converted to 1.2 V for the digital part and 1.5 V for the analogue part of the front-end electronics. A ribbon cable establishes the connection to the single chip support card that carries the front-end chip (I3 or I4). For chips connected to a sensor a depletion voltage can be applied via a LEMO 00 connector.
The graphical user interface software utilized is STcontrol. This program provides the settings of the scan configuration and automated analysis with graphic representation of

[1]Field-Programmable Gate Array
[2]Static Random-Access Memory
[3]Low-Voltage Differential Signaling
[4]Complementary Metal-Oxide-Semiconductor

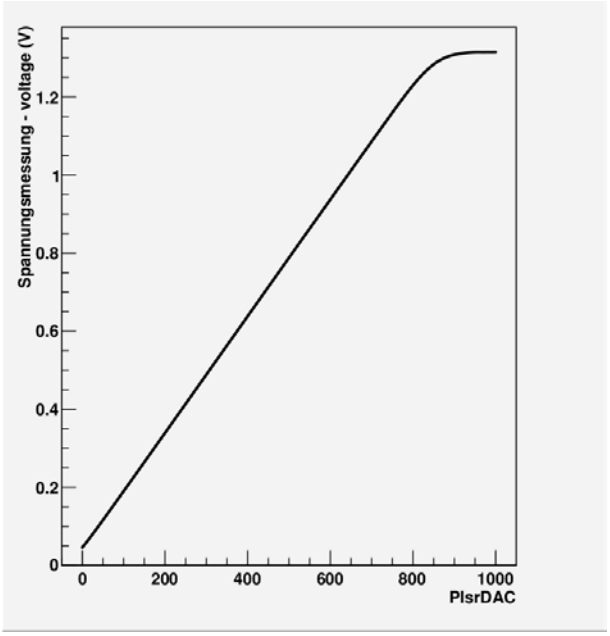

Figure 4.3.: V_{cal} vs. *PlsrDAC*

the obtained data. Scan routines with loops over up to three different parameters as well as predifined scan types can be initialized by STcontrol. The chip configuration can be stored and loaded automatically.

4.2. Calibration of the chip before the analysis

To determine the exact correlation between *PlsrDAC* and V_{cal} the voltage applied on the capacitors for test charge injection was measured by an external voltmeter. The data points are plotted in a graph with the corresponding *PlsrDAC* value on the abscissa (see Figure 4.3). For high *PlrsDAC* values the voltage reaches a saturation value. A linear regression on the straight part of the data points gives $\Delta V_{\text{cal}}/PlsrDAC$ step = 1.495 mV. This value is saved in the chip configuration as *VCAL grad.*. It allows for a precise estimation of the charge injected by the capacitors.
Since the chip is connected to a sensor, to avoid influences of the sensor on the charge injected into the electronics, the sensor has to be depleted by an external voltage. An undepleted sensor would establish a connection between adjacent pixels thus falsifying the signal that is read out. Furthermore, the capacity of a depleted sensor is lower. The depletion voltage applied in this analysis is 100 V.

The discriminator threshold is tuned automatically to a constant value for all pixels in order to have a gauged discriminator response.

4.3. Information on the chip used for the analysis

For the analysis an FE-I4A was used, where the "A" stands for the first version that was fabricated (for a detailed description see [14]). In the first and last columns of this chip generation different electronics than on the rest of the chip were implemented. Since these parts do not operate satisfactorily, they will not be carried over to the final version of the FE-I4. Therefore, for this analysis the double-columns 1, 2, 39 and 40 have always been deactivated.
The pixels with the following coordinates (column, row) are known to be broken: (44-45, 278-279), (49, 234), (54, 59), (39, 121). The pixels (23-30, 0), (35-42, 0) and (47-54, 0) are out of work for technical reasons.

5. Development of a *PrmpVbpf-FdacVbn* tuning

The time over threshold (ToT) is subject to many input parameters. It depends on the input charge of the preamplifier, the threshold of the discriminator and the preamplifier feedback current.
The front-end chip should be tuned to have a uniform response to a standardized input. Due to the small range of the ToT (only 14 different values), a balanced decision must be taken between the possibility of choosing a high resolution on small amounts of charge (and losing the information at large charges because of overflow) or a low resolution including also high-charge impacts. At this point, it must be taken into account that, according to the LANDAU distribution (see Chapter 3.1.1), large deposited charges are very improbable.
The purpose of this chapter is to present an automated and fast-working strategy to tune the chip in such a way that a pre-specified charge quantity results in a chosen ToT response.
Since the discriminator threshold is usually chosen as low as possible – depending on the detector noise – it can be disregarded in this analysis. It is merely necessary to tune all pixels of the chip to the same threshold. Throughout the examination, a threshold of 3 000 electrons was applied.
As the input charge and the resulting ToT are given parameters, it is necessary to find the best combination of the parameters *PrmpVbpf*, *FdacVbn* and *FDAC* (which control the feedback current) for the optimization. Since 8 bit $\times$ 8 bit $\times$ 4 bit corresponds to 2^{20} = 1 048 576 combinations, it is evidently impossible to scan all these combinations picking the best one at the end. Therefore, a method that works with substantially less input data is required.

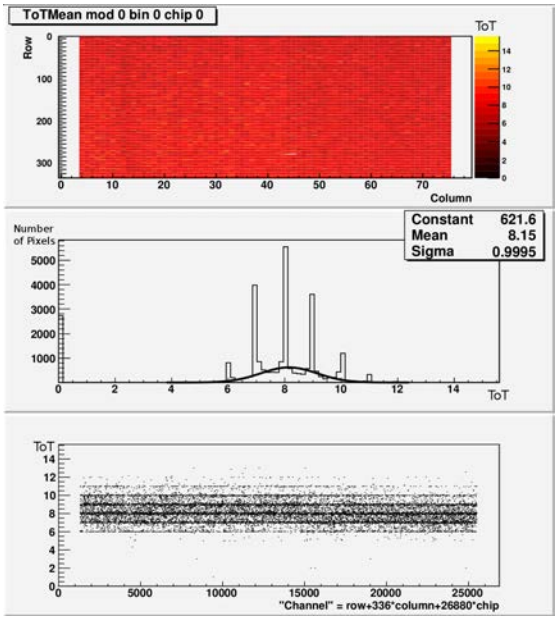

Figure 5.1.: Typical ToT distribution with untuned *TDAC*.

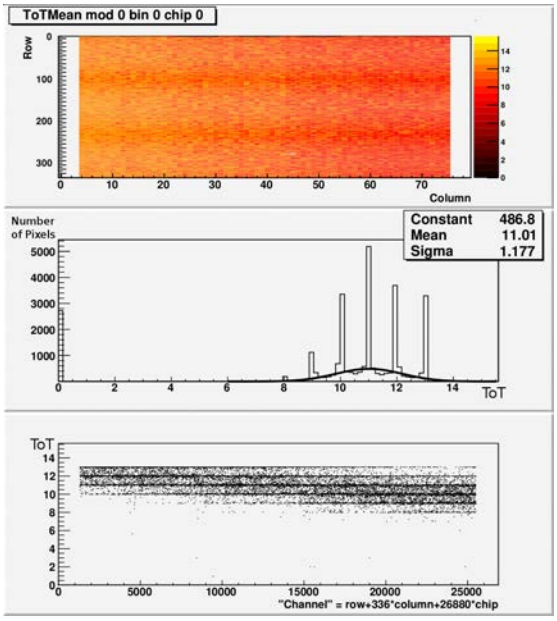

Figure 5.2.: The overflow peak at ToT = 13.

5.1. ToT verification scans

In the following analysis mainly data obtained from so-called "ToT verification scans" was used. In this kind of scan, a predefined amount of charge from the test charge capacitors is injected in the amplifier-discriminator circuit and the resulting ToT is recorded. The ToT is always given in units of 25 ns. In other words, a ToT of 1 corresponds to 25 ns, a ToT of 5 corresponds to 125 ns.

During the first measurement series, in order to get a precise determination of the average ToT, the procedure was repeated 200 times for every pixel. In the later measurements this number was progressively reduced to 25 repetitions without any loss in precision. In Figure 5.1 the resulting distribution of ToT on the chip is shown.

Two data sets were taken, one with 20 000 electrons injected and the other with 10 000 electrons injected. The following discussion refers to the measurement with 20 000 electrons, the most meaningful results for 10 000 electrons can be found in Appendix A.

The peaks shown in the histogram in the central part of Figure 5.1 derive from the averaging process. Usually a pixel gives the same integral ToT value in case of the same charge. Thus the average ToT also amounts to the same integral value. Where the falling edge of the discriminator signal is close to the boundary between two 25 ns blocks, pixels

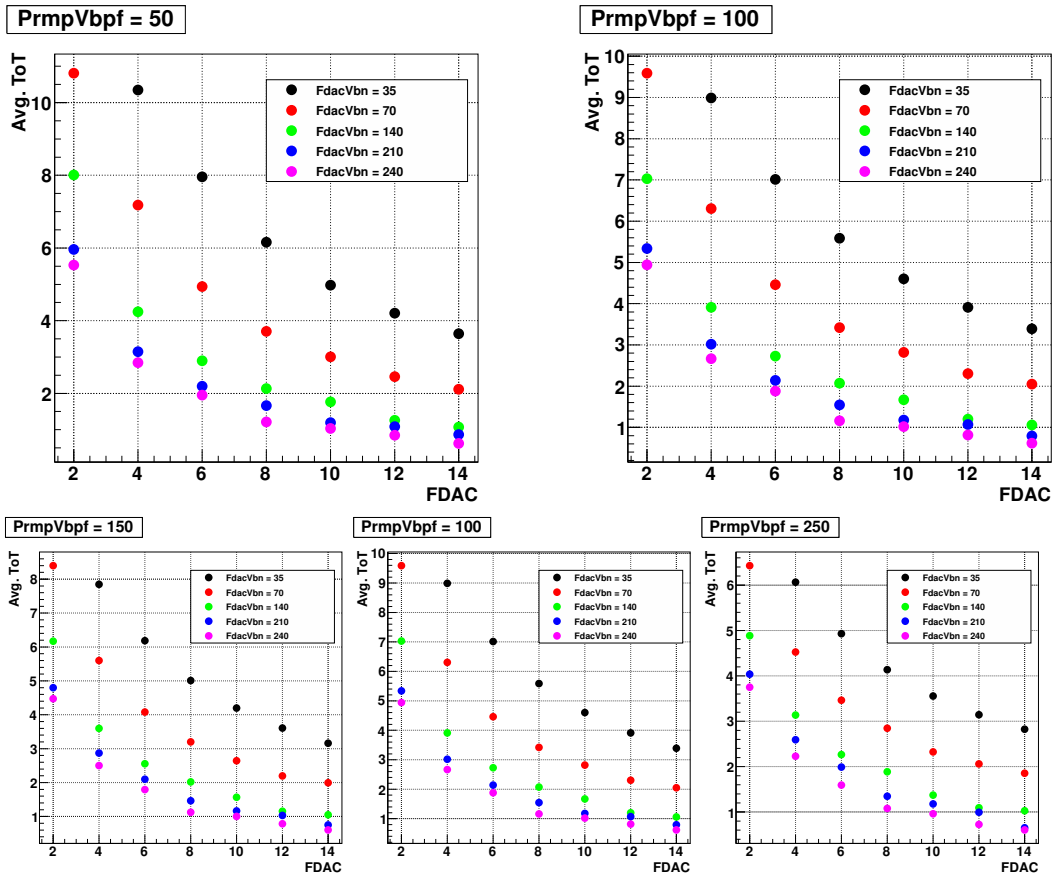

Figure 5.3.: The average ToT at different configurations of the feedback current parameters.

in some cases may be assigned to the longer and in some cases to the shorter ToT, thus resulting in a non-integral average ToT. Since such constellations are not very likely, most of the pixels have an integral average ToT value. Hence the ToT distribution shows peaks at integral numbers. The peak at ToT = 0 is caused by the deactivated columns that do not return any read-out data.

The overall arithmetic mean is stored in graphs like those in Figure 5.3 in order to have an overview on the effects of the parameters *FDAC*, *PrmpVbpf* and *FdacVbn*. Due to the large quantity of data points, the errors are small ($\sigma_{\mathrm{ToT}}/\mathrm{ToT} \lesssim 2 \cdot 10^{-3}$) and the errorbars are overlaid by the markers.

5.2. The change in ToT with reference to *FDAC* and *FdacVbn*

From the plots in Figure 5.3, the basic assumption, viz., that the feedback current increases with increasing *FDAC*, *PrmpVbpf* and *FdacVbn* and thus the ToT decreases, can be confirmed.
As a consequence of the fact that *FdacVbn* gives the *FDAC* step size, the change of ToT (δToT) could be expected to be constant in *FDAC*. But a graphical representation (see Figure 5.4) of the decrease of the ToT shows that δToT depends much more on *FDAC* than on *FdacVbn*. Especially at high *FDAC* values, a systematical behaviour of the data points cannot be identified. Therefore, this approach was not followed.

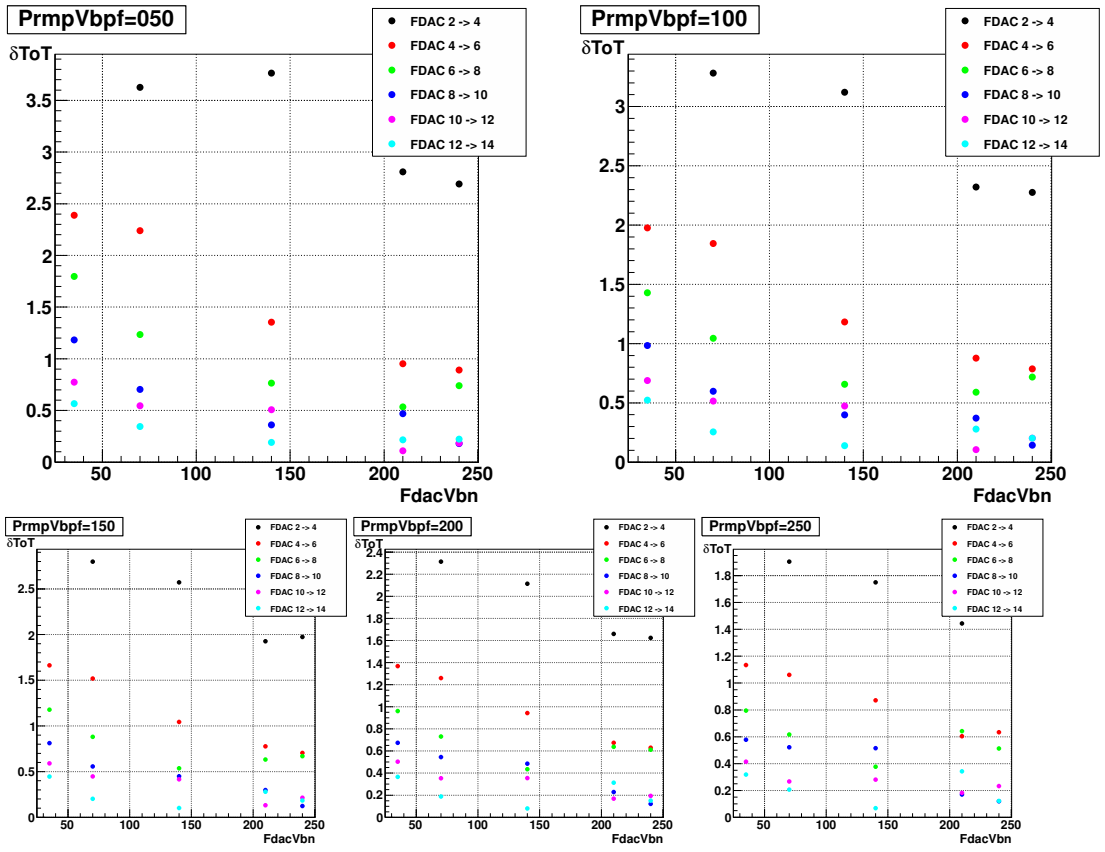

Figure 5.4.: The change in ToT in different regions of *FdacVbn*.

5.3. Analytical approach to describe the ToT

Starting from the assumption that the feedback current depends on *FDAC* and *PrmpVbpf* while *FdacVbn* is the *FDAC* step size, the feedback current I should obey the following equation:

$$I \propto \underbrace{PrmpVbpf}_{=:P} + \underbrace{FdacVbn}_{=:F} \cdot \underbrace{FDAC}_{=:x} \; . \tag{5.1}$$

For reasons of simplification, the parameters will be replaced by x, P and F in formulas. In an approximation for high charge quantities, the time-walk effect can be neglected and the rising edge of the preamplifier output signal is assumed to be vertical. Thus the time over threshold is given by

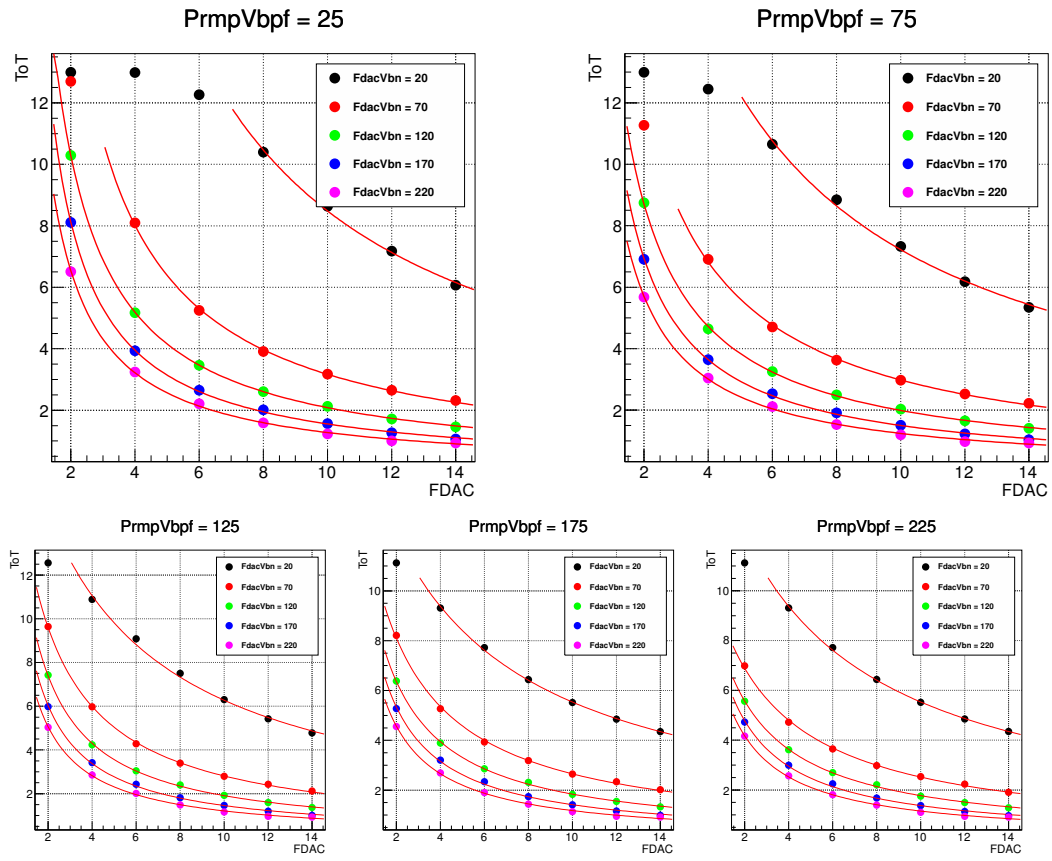

Figure 5.5.: The average measured ToT and the fit function $f(x)$.

$$\begin{aligned} \mathrm{ToT} &= \frac{Q - Q_{\mathrm{thresh}}}{I} = \frac{Q'}{I} = \frac{Q'}{P + F \cdot x} \\ &= \frac{Q'/F}{P/F + x} = \frac{a}{b + x} = f(x) \end{aligned} \tag{5.2}$$

with $a = Q'/F$ and $b = P/F$.

The determined function for the ToT estimation fits very well to the data (see Figure 5.5). Data points with ToT > 11 were not taken into account because of overflow effects. As Figure 5.2 shows, already at an average ToT of 11 a significantly high overflow is collected in the bin at ToT = 13, thus biasing the average value. Moreover, only the first data point with ToT < 1 is utilized to fit the function while all following points are discarded (the second criterion is only met in the measurement series with 10 000 electrons, see Appendix A). The average ToT tends to zero much faster than the fit function in this region.

The fit parameter $a = Q'/F$ should not change for all graphs with the same *FdacVbn* value. Furthermore, a should decrease hyperbolically when plotted against *FdacVbn* and it should be independent of *PrmpVbpf*. In Figure 5.6 a is plotted versus *FdacVbn*. The function fitted to the data is

$$f_a(F) = \frac{k_0}{F - k_1} + k_2 \tag{5.3}$$

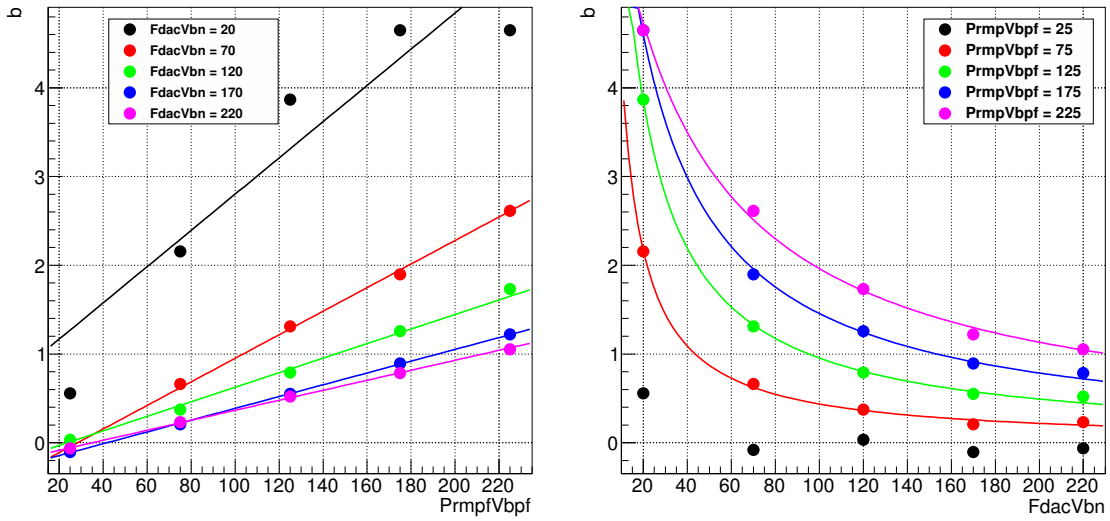

Figure 5.7.: The parameter b compared to the fit functions $f_b^1(P)$ and $f_b^2(F)$.

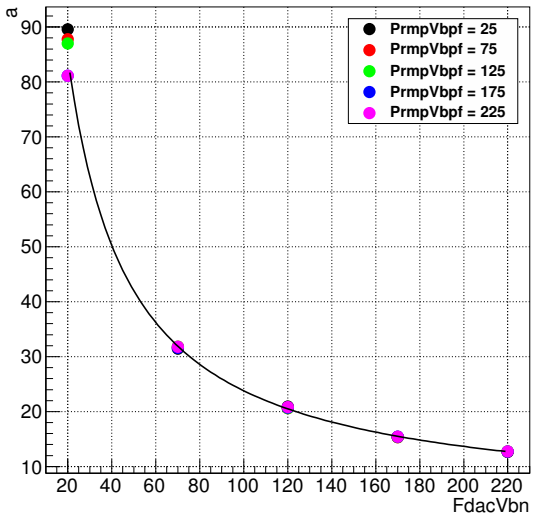

Figure 5.6.: $f_a(F)$ fitted to the parameter a obtained from the fits in Figure 5.5.

The errors on the fit are very small, $\sigma_{k_i}/k_i < 10^{-5}$ in this example. The higher dispersion at $PrmpVbpf = 25$ derives from the overflow effects and the resulting lower number of data points fitted.

The parameter b is expected to be linear in $PrmpVbpf$ and inversely proportional to $FdacVbn$. The plots in Figure 5.7 demonstrate that the dependency on two variables

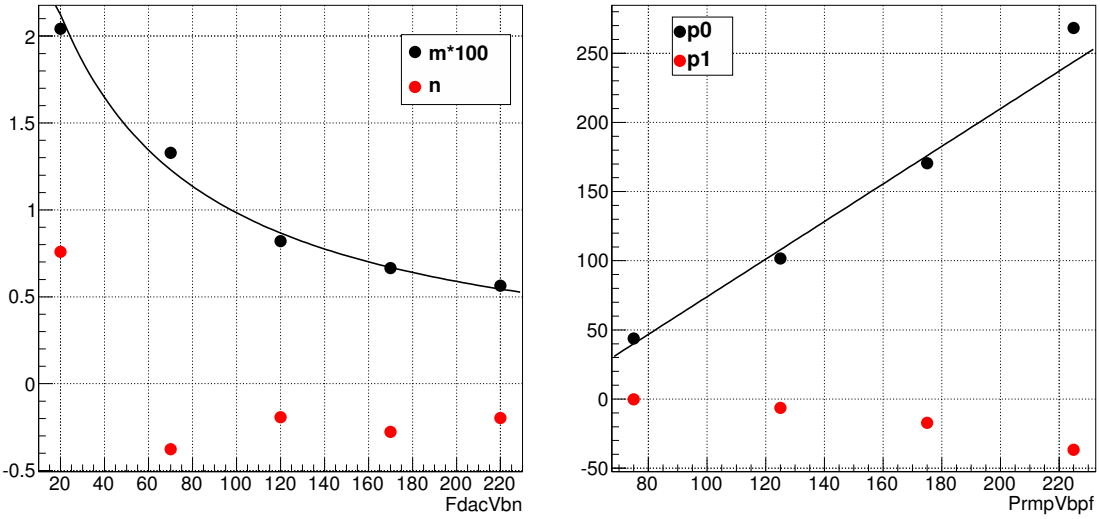

Figure 5.8.: The parameters of the functions $f_b^1(P)$ and $f_b^1(F)$ obtained from the fits in Figure 5.7.

causes higher inaccuracies. The absolute errors are of about 0.02 for the data points at $FdacVbn = 20$ and smaller than 0.01 for the other data sets. The data points in the plots are fitted to a function $f_b^1(P)$ (left side) and $f_b^2(F)$ (right side):

$$f_b^1(P) = m \cdot P + n \,, \qquad f_b^2(F) = \frac{p_0}{F - p_1} \,, \tag{5.4}$$

with m, n, p_0 and p_1 as free parameters. For the data set $PrmpVbpf = 25$ the fit did not converge adequately. Furthermore, the data set of $FdacVbn = 20$ cannot be confirmed to be linear in *PrmpVbpf*. In Figure 5.8 the parameters of $f_b^1(P)$ and $f_b^2(F)$ are depicted. While m (representing $1/FdacVbn$) fits to a hyperbola, the linearity of p_0 (representing *PrmpVbpf*) cannot be confirmed, more data points would be required to make a clear decision. The parameters n and p_1 can be considered as an offset which should be constant. As the present plots show that this is not the case, a precise mathematical link between *PrmpVbpf*, *FdacVbn* and the fit parameter b cannot be established. For this reason, no further study on the linearity of p_0 was conducted.
Although the parameter b is subject to higher fluctuations and a precise relation between b and the chip parameters cannot be found, the function $f(x)$ fits well to the data.

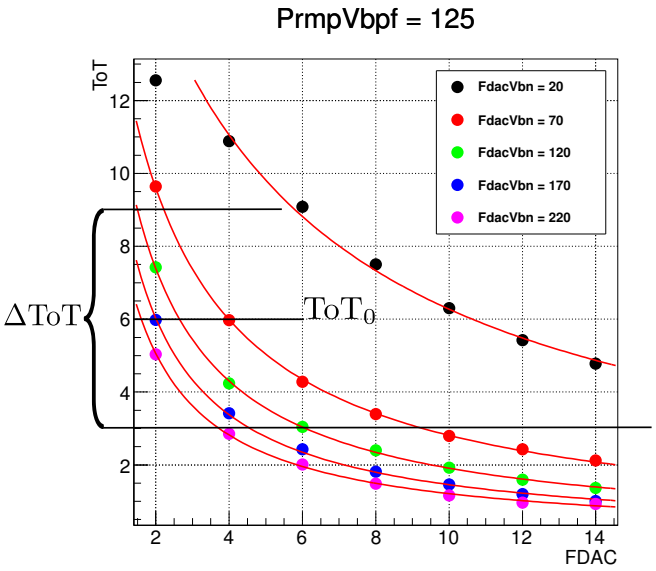

Figure 5.9.: Example for the choice of ToT_0 and $\Delta\mathrm{ToT}$.

5.4. Determination of the best parameter configuration

As the plot in Figure 5.9 demonstrates, the slope of the ToT curve is very steep for small *FDAC* values. In this region the ToT decreases by more than 1 ToT unit per *FDAC* step. Since *FDAC* should be used to calibrate the ToT, such big ToT steps are not desired because of the risk that the target ToT cannot be reached. In other words, the resulting ToT for a certain *FDAC* may be too long by one ToT unit and the resulting ToT at *FDAC* increased by one may already be too short by one ToT unit. This scenario must be avoided and thus a cut for the useful *FDAC* values must be made at $FDAC \sim 3 - 4$.
As shown before, the function

$$\mathrm{ToT} = f(x) = \frac{a}{b + x}$$

is suitable to describe the dependency of the ToT on *FDAC*. The dependence on two parameters implies that only two points of the curve must be fixed to specify the function parameters.
The desired ToT (ToT_0) and the ToT range over which it should be possible to shift the ToT ($\Delta\mathrm{ToT}$) together with the minimum and maximum suitable *FDAC* value are the conditions to the desired function. ToT_0 lies in the middle of the $\Delta\mathrm{ToT}$ range. The maximum *FDAC* (x_{max}) is 15, the minimum (x_{min}) is 3 or 4. Thus, the parameters a and b are given by

$$a = (x_{\min} - x_{\max}) \left[\frac{1}{\mathrm{ToT}_0 - \frac{1}{2}\Delta\mathrm{ToT}} - \frac{1}{\mathrm{ToT}_0 + \frac{1}{2}\Delta\mathrm{ToT}} \right] \tag{5.5}$$

$$b = \frac{\mathrm{ToT}_0}{\Delta\mathrm{ToT}}(x_{\max} - x_{\min}) - \frac{x_{\max} + x_{\min}}{2} \tag{5.6}$$

with the conditions

$$f(x_{\min}) = \mathrm{ToT} + \frac{\Delta\mathrm{ToT}}{2}\ , \quad f(x_{\max}) = \mathrm{ToT} - \frac{\Delta\mathrm{ToT}}{2}\ . \tag{5.7}$$

Certainly not every combination of ToT_0 and ΔToT can be realized, the parameters a and b must always be in the range that is given by the plots in Figure 5.6 and 5.7 (here ~15 - 80 for a and ~0 - 4.5 for b). ΔToT should be chosen large, in order to have a wide range for the tuning. But if it is too large, the slope of the curve may become too steep at small *FDAC* and thus the spacing in ToT may become too wide. Therefore a balance must be struck between a large ΔToT and small steps in ToT.
Once the desired parameters a and b have been determined, they can be compared to the parameters a and b obtained from the fit to the data.
The fit function in Figure 5.6 allows for the determination of the desired *FdacVbn* value. The inverse fit function gives the desired *FdacVbn* value for a fixed a.
The determination of *PrmpVbpf* is more difficult because it depends on two variables. As seen above, an analytical description for b depending on *PrmpVbpf* and *FdacVbn* cannot be infered. But *FdacVbn* is already known. Thus, by taking another set of measurements at fixed *FdacVbn* and different *PrmpVbpf* values the dependence of b can be reduced to only one parameter. The parameter b of these additional data sets is plotted versus *PrmpVbpf* in Figure 5.10. From a linear fit to this data the corresponding *PrmpVbpf* for a fixed b can be derived.
With the knowledge of the two parameters *PrmpfVbpf* and *FdacVbn* an existing *FDAC* tuning routine is started that brings all pixels to the desired ToT. As an example a tuning with the taken data sets (Figure 5.5) for 20 000 electrons to ToT = 6 and ToT = 8 was realized. For the resulting ToT distribution after the *FDAC* tuning see Figure 5.11. The higher dispersion at a target ToT of 8 may be a consequence of the larger ToT step sizes at the chosen combination of ToT_0 and ΔToT.
For the result of a tuning with 10 000 electrons see Figure A.5 in Appendix A.

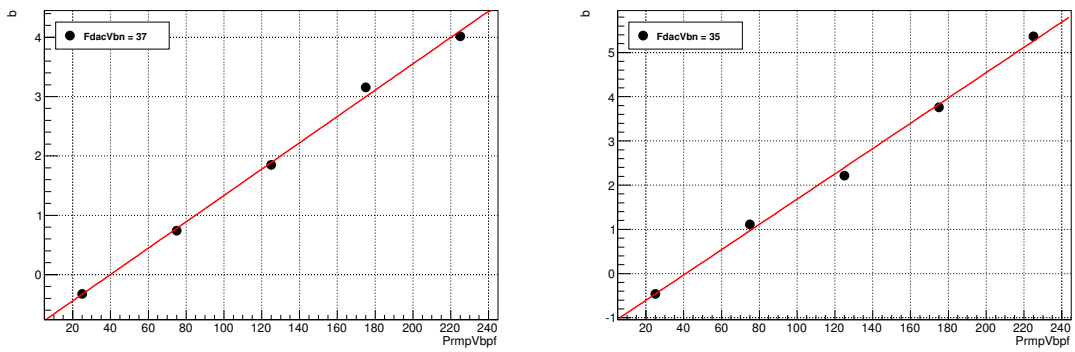

Figure 5.10.: The parameter *b* with the fit for the determination of *PrmpVbpf*. The target ToT is 6 (left) and 8 (right).

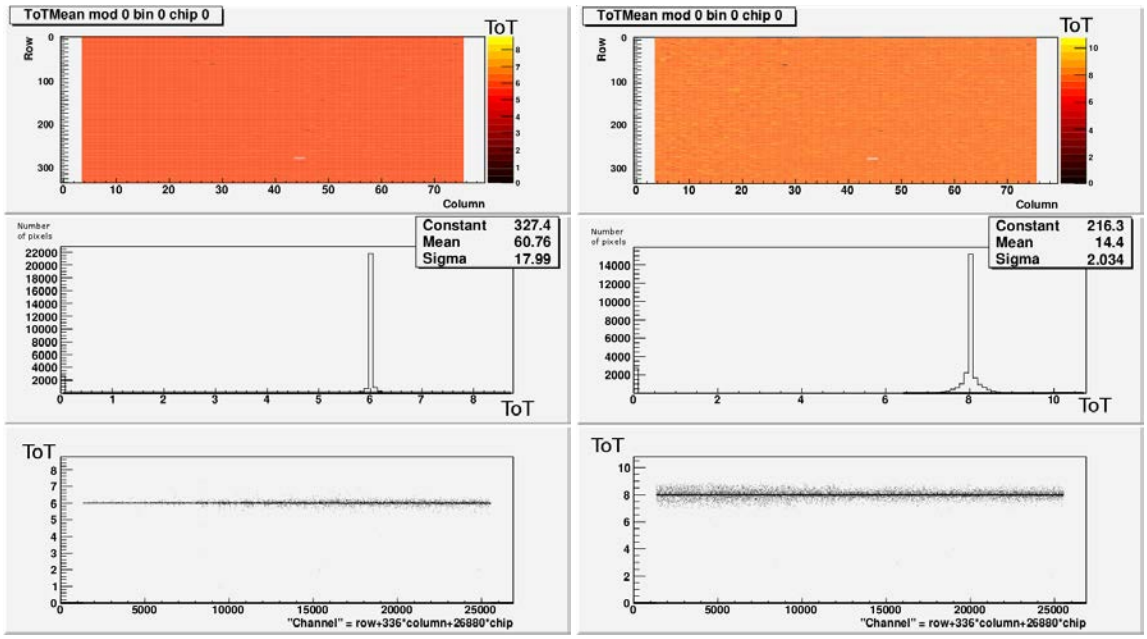

Figure 5.11.: ToT distribution for 20 000 electrons after a tuning to a ToT 6 (left) or 8 (right).

5.5. Estimation of the scan-time

In the conducted analysis, data points at five different values for *PrmpVbpf* and *FdacVbn* and for seven different *FDAC* values were taken. In order to have a good fit of the parameters a and b, the number of *PrmpVbpf* and *FdacVbn* data points should not be reduced. For *FDAC*, five different data points would be enough for a good fit of $f(x)$, since the errors of a and b are very small. For a rough estimation of the scan time, two complete scans with ten injections in every pixel were realized. Since 10 injection $\times$ 26 880 pixels are 268 800 data points, the resulting mean value is still very accurate. Five different values for *PrmpVbpf* and *FdacVbn* were chosen. For *FDAC*, seven different values were scanned in the first run and five in the second run. The resulting scan time is 38.5 min in the first run and 26.5 min in the second run. Adding 20% of the scan time to approximate the duration of the extra scan for the determination of b, the overall scan time is roughly 46 min and 32 min. The runtime of the fitting routines is only a few seconds and can be neglected.
Additionally, 3.5 min must be added for the *FDAC* tuning, to get the time of a complete feedback current tuning.

6. Time-walk and in-time threshold

Since the time-walk effect cannot be eliminated, it must be taken into account in the further signal processing. The following sections will give an overview of the methods used to characterize the time-walk and how the in-time threshold is determined.

6.1. t_0-Scan

The t_0-scan is a routine that prepares the FE configuration for a subsequent time-walk measurement or in-time threshold scan. For this scan a test charge is injected to the preamplifier. The test charge is chosen much higher than the threshold to be sure that the time-walk is negligible. The varying parameters in this scan are *Strobe delay* and *Trigger delay*. The *Strobe delay* shifts the strobe signal in steps of ~1 ns forwards in time, the *Trigger delay* shifts the trigger signal for the read-out of the chip by 25 ns. The preset scan configuration in the STcontrol software shifts the *Strobe delay* over the whole 6-bit range from 0 to 63, the *Trigger delay* is shifted from 55 to 58 (this is the convenient time window for a readout). The injection procedure is repeated 25 times for every pixel. For every injection it is recorded whether a hit was registered or not. Hits are only registered if the rising edge of the discriminator signal falls within the time interval that is requested by the trigger. From the obtained data, graphs like the one in Figure 6.1 are automatically created.
The interesting part of the obtained data is the rising edge of the hit occupancy. The point where the hit occupancy reaches half of the maximum is considered to be the threshold for registering an event in this trigger interval. Assuming that the hit occupancy at the rising edge has the shape of an "S-curve" [17], the following function can be fitted to the data points:

$$\frac{A}{2} \cdot \mathrm{Erfc}\left(\frac{x - x_{\mathrm{thresh}}}{B}\right), \tag{6.1}$$

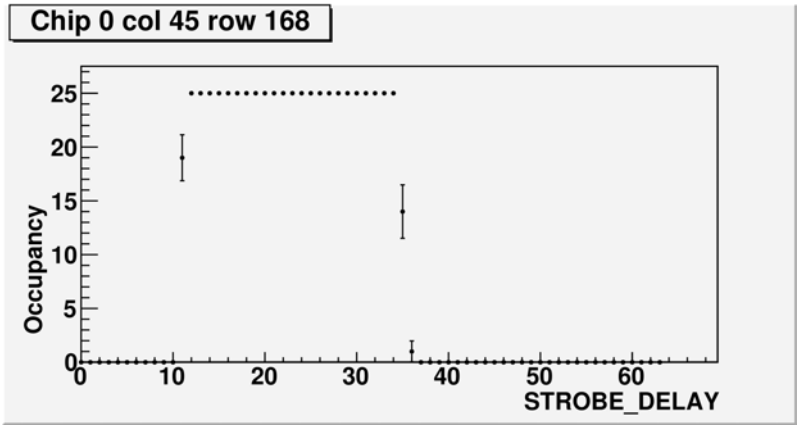

Figure 6.1.: Occupancy in a t_0-scan for the pixel in column 45 and row 168 at a trigger delay of 56.

where A denominates the maximum occupancy, Erfc(x) is the complementary error function[1], x corresponds to the *Strobe delay*, x_{thresh} to the 50% occupancy point and B is a noise-related smoothing of the S-curve's edge.

Most of the data sets ($\sim$ 90%) fit to the function, thus x_{thresh} can be determined from the fit parameters. But in some constellations the fit does not converge satisfactorily. An investigation on the data sets that do not fit reveals that, first of all, graphs without intermediate data points or with two symmetrically arranged intermediate data points are involved.

For these graphs an alternative routine for the determination of the *Strobe delay* threshold was implemented by fitting a linear function to the rising edge. The point where this function crosses half the maximum value is then considered to be the *Strobe delay* threshold. The resulting threshold of a t_0-scan with and without the alternative fit routine implemented can be compared in Figure 6.2. To abbreviate the scan time, only one pixel out of six is read out since this sample is still large enough. While on the left side several pixel in the zigzag-strip pattern[2]are missing, on the right side all pixels have a correct threshold value (except for inactive and broken pixels).

From the results of the t_0-scan the best *Trigger delay* and the *Delay cal.* value are automatically calculated. The *Delay cal.* value gives an exact step size of *Strobe delay* in ns, that lies close to 1 ns. It is calculated by comparing the position of the rising edge of the occupancy in data sets with different *Trigger delay* settings. These two parameters are automatically written into the module configuration and allow for subsequent time-walk and in-time threshold scans.

[1] $\text{Erfc}(x) = \frac{2}{\sqrt{\pi}} \int_x^\infty e^{-\tau^2} \, \mathrm{d}\tau$

[2] This pattern is a consequence of the applied read-out mask.

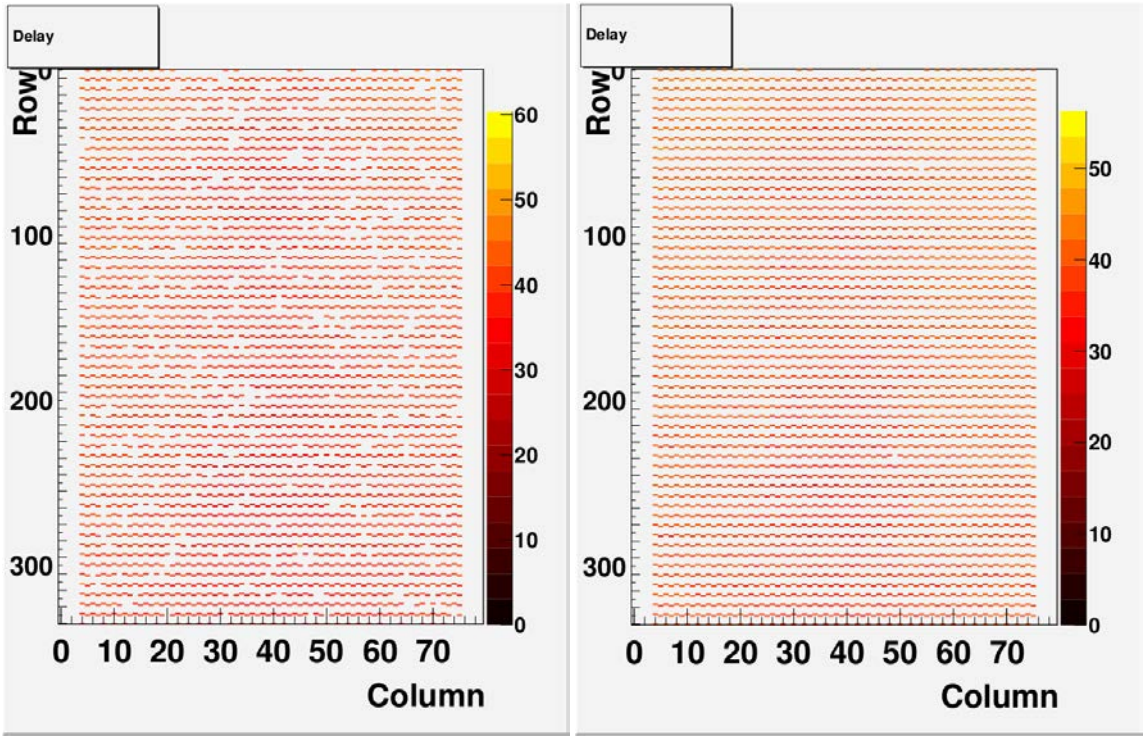

Figure 6.2.: *Strobe delay* position of the rising edge from a t_0-scan without (left) and with (right) the alternative fit routine at *Trigger delay* = 57.

6.2. Time-walk measurement

The time-walk measurement is a scan routine that automatically determines the time-walk at different amounts of charge. A prerequisite to this scan is a previous t_0-scan to determine the optimal *Trigger delay* and the *Delay cal.* value.
In the inner scan loop the *Strobe delay* is shifted from 0 to 63. In the outer scan loop V_{cal} is increased in 25 steps from 70 to 1000. For every amount of charge the resulting maximum *Strobe delay* is calculated as described above.
The graph in Figure 6.3 shows the maximum *Strobe delay* at which the signal is still detected. At large amounts of charge (*PlsrDAC* > 400), the rising edge of the preamplifier output is nearly vertical and the time-walk tends to zero. Therefore, the curve tends towards a limiting value. The time-walk is given by the delay difference to the maximum delay. The saturation effects of V_{cal} at high *PlsrDAC* ($\gtrsim$ 800) values do not seem to have any effect on the time-walk.
During the analysis, it became apparent that the *Trigger delay* chosen by the t_0-scan routine is not automatically suitable for the time-walk analysis. The trigger signal is sent too early for a measurement of large time-walks at small amounts of charge (see Figure 6.4). As a result, the lower part of the curve for *PlsrDAC* < 100 (corresponding to ~5300 electrons) is cut off. Therefore, the critera for the selection of the *Trigger delay* must be revised. Figure 6.3 shows the graph for the measurement with a *Trigger delay* increased manually by 1.

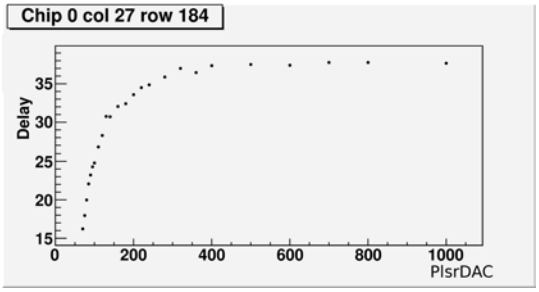

Figure 6.3.: Time-walk measurement with the corrected *Trigger delay*. The unit of the delay is ns.

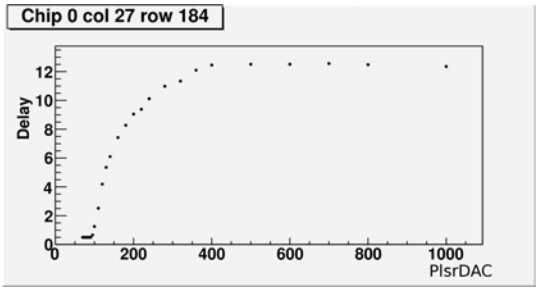

Figure 6.4.: Time-walk measurement with the *Trigger delay* chosen by the t_0-scan routine. The unit of the delay is ns.

6.3. In-time threshold

The in-time threshold is the amount of charge that causes a time-walk of 25 ns. To be on the safe side, the in-time threshold is defined as the charge that causes a time-walk of 20 ns [17].

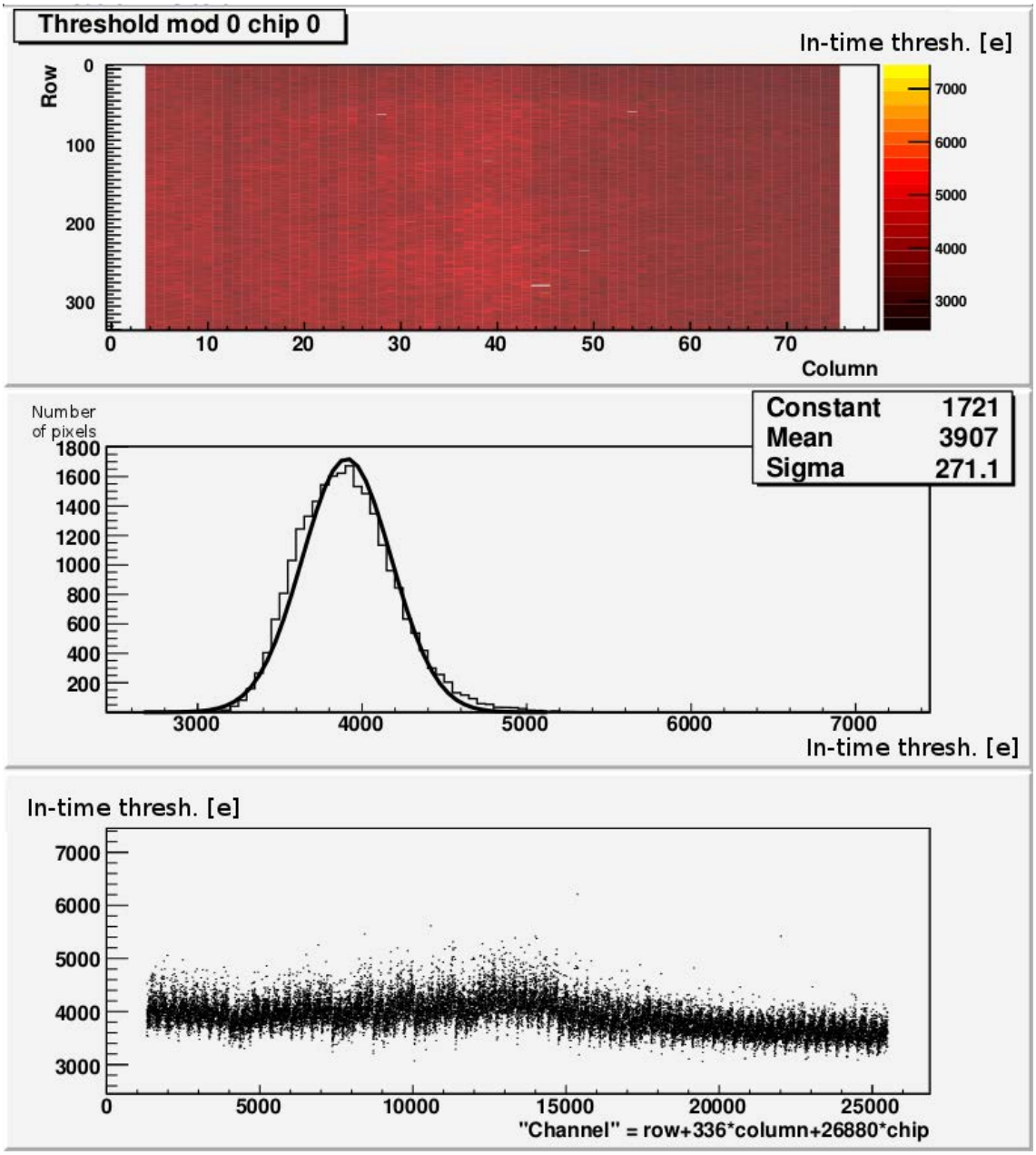

Figure 6.5.: Distribution of the in-time threshold, for details see text.

For an in-time threshold scan the *Strobe delay* is set to the threshold value obtained from the t_0-scan minus 20 ns. Then *PlsrDAC* is increased from 0 to 200 registering if the signal is recorded at the corresponding trigger delay. For every pixel 100 measurements at each *PlsrDAC* value are taken. For a time-walk > 20 ns the signal is assigned to the next bunch crossing. Thus, the determined threshold gives the amount of charge at which the signal is detected in time by the discriminator.
The in-time threshold at a global threshold of 3 000 electrons with *PrmpVbpf* = 20, *FdacVbn* = 50 and *FDAC* = 7 is shown in Figure 6.5. Since *FDAC* was not tuned in this measurement, the feedback current is not constant for all pixels. Due to time constraints, it was not possible to examine if a tuned feedback current reduces the dispersion of the in-time threshold.

7. Summary and Outlook

7.1. *PrmpVbpf-FdacVbn* tuning

A function that is suitable to describe the dependence of the ToT on *FDAC* could be found during this analysis. Also the dependence on *FdacVbn* can be determined very accurately by this function. But for an automated determination of *PrmpVbpf*, due to the higher dispersion of the fit parameter *b*, an additional measurement, which increases the overall scan time by 20%, is inevitable. Nevertheless, a scan time of 32 min is still reasonable.
The tunings of 20 000 electrons to a target ToT of 6 and 8 (and the tuning of 10 000 electrons to a target ToT of 6, see Figure A.5) were successful. The response of the chip is nearly homogeneous and the outliers are accumulated close to the target ToT.
But for a verification of this tuning strategy, more measurements must be taken. In the context of this thesis project, due to the limited time frame, it was not possible to implement the developed tuning strategy in an automated USBpix scan routine. Since the "hand made" acquisition of the data for the tuning takes ~2 hours for a single tuning an automated tuning is indispensable for a thorough validation.
Further examinations are required, especially at charges close to the discriminator threshold and at extreme target ToTs close to 0 or 13. Also the tuning quality at the minimum and maximum of the *PrmpVbpf* and *FdacVbn* range must be verified.

7.2. Time-walk and in-time threshold

The determination of the rising edge of the occupancy in a t_0-scan was completed by introducing an alternative fit routine, which is based on a linear fit. This allows for a correct determination of the *Strobe delay* threshold for all data sets that cannot be fitted satisfactorily with an S-curve.
The data obtained from the time-walk measurement shows the expected rising curve that tends to a limit at high charges. Furthermore, it reveals that the criteria for the best *Trigger delay* in the t_0-scan must be revised, because the automatically chosen *Trigger delay* does

not offer a sufficiently wide range for the *Strobe delay*.
The measurement of the in-time threshold works properly, but for the characterization of the in-time threshold, more measurements at a tuned feedback current are required.

A. Appendix

A.1. Measurement series with 10 000 electrons

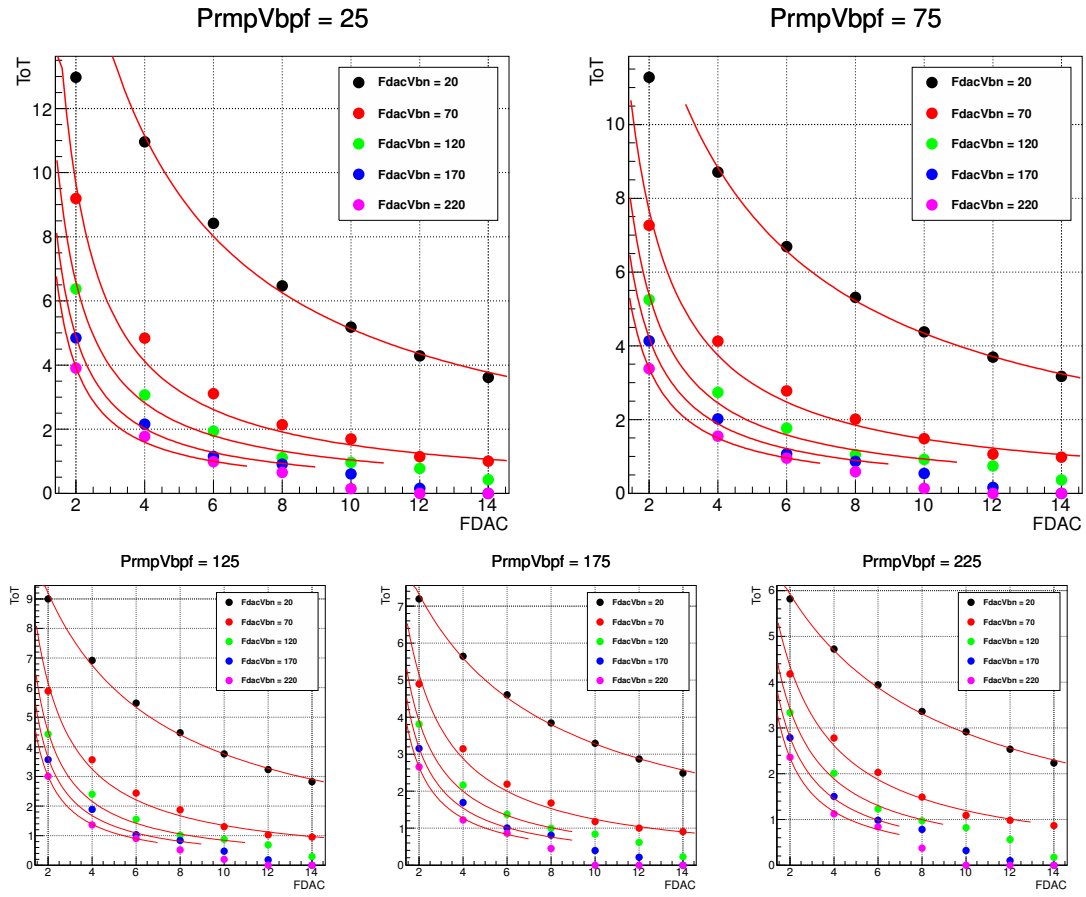

Figure A.1.: The average ToT measured and the fit function $f(x)$.

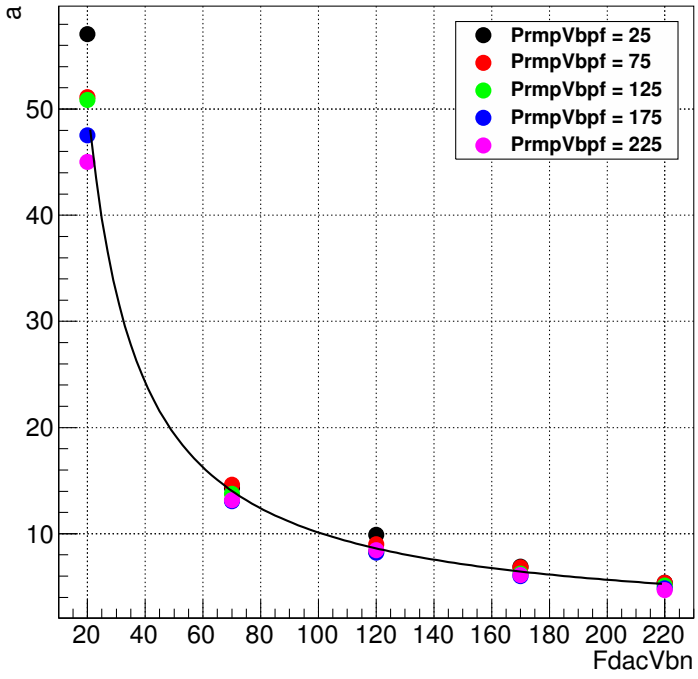

Figure A.2.: f_a fitted to the parameter a obtained from the fits in Figure A.1.

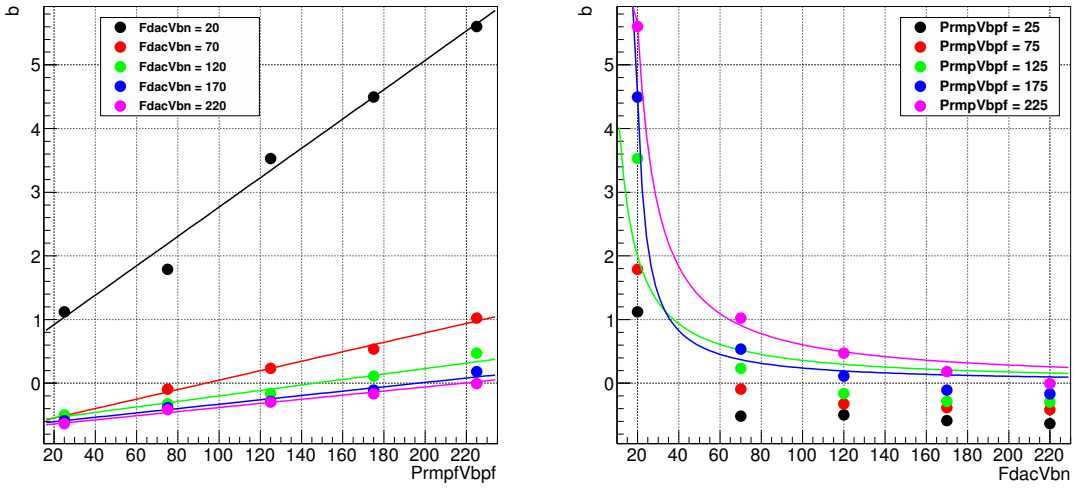

Figure A.3.: The parameter b obtained from the fits in Figure A.1 compared to the fit functions $f_b^1(P)$ and $f_b^2(F)$. At $PrmpVbpf = 25$ and 75 the fit with $f_b^2(F)$ did not converge.

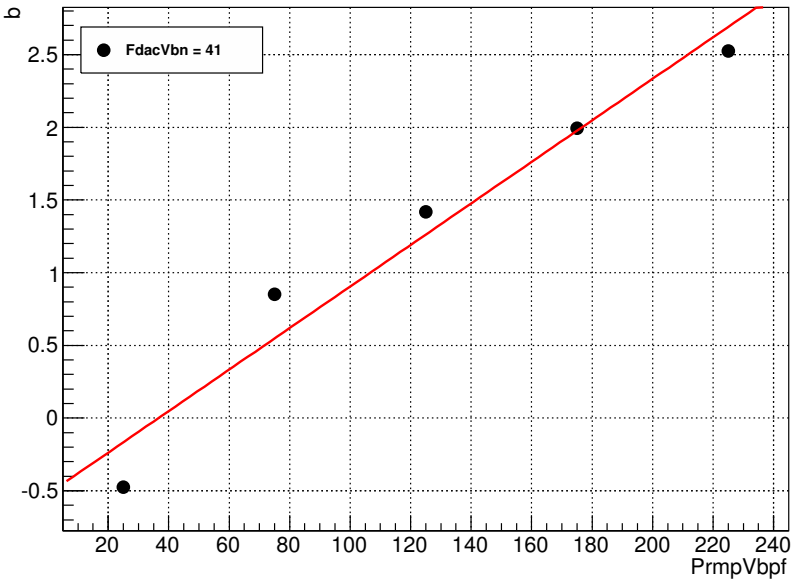

Figure A.4.: The parameter *b* with the fit for the determination of *PrmpVbpf*. The target ToT is 6.

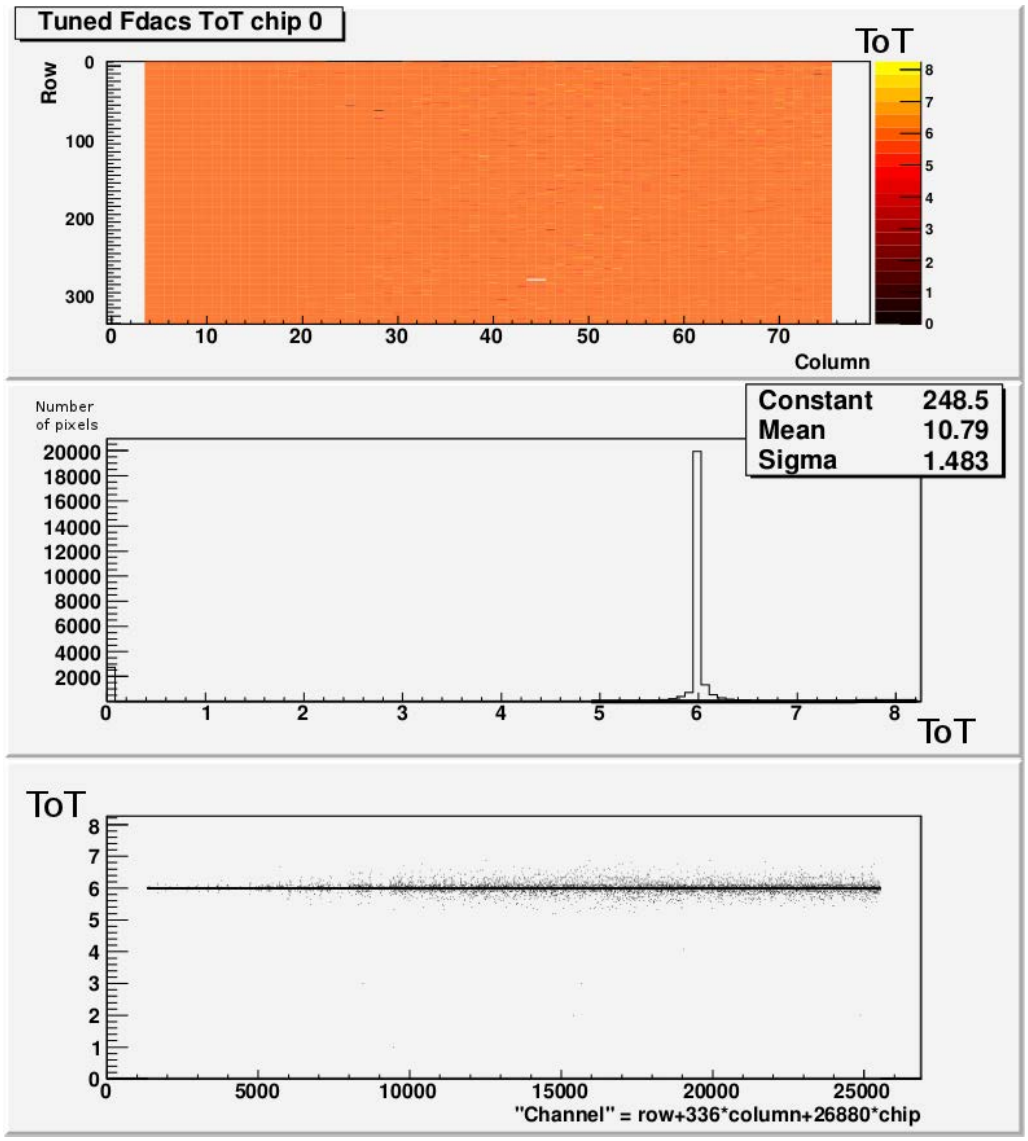

Figure A.5.: ToT distribution for 10 000 electrons after a tuning to a ToT of 6.

Bibliography

[1] O. Brüning et al. LHC Design Report. (CERN-2004-003-V2), 2004.

[2] ATLAS Collaboration. ATLAS DETECTOR AND PHYSICS PERFORMANCE Technical Design Report. (CERN/LHCC 99-14), 1999.

[3] ATLAS Collaboration. The ATLAS Experiment at the CERN Large Hadron Collider. *Journal of Instrumentation*, 3(2008 JINST 3 S08003), 2008.

[4] ATLAS IBL Community. Insertable B-Layer Technical Design Report. (CERN-LHCC-2010-013), 2010.

[5] Heinz Pernegger. The ATLAS Insertable B-Layer Pixel Detector. *Proceedings of Science*, Vertex 2011(PoS (Vertex 2011) 018), 2011.

[6] Joao Pequenao. http://cdsweb.cern.ch/record/1095924, 2008.

[7] G. Aad et al. ATLAS pixel detector electronics and sensors. *Journal of Instrumentation*, 3(2008 JINST 3 P07007), 2008.

[8] Joao Pequenao. http://cdsweb.cern.ch/record/1095925, 2008.

[9] Gerhard Lutz. *Semiconductor Radiation Detectors: Device Physics*. Springer, 1999.

[10] Leonardo Rossi, Peter Fischer, Tilman Rohe, Norbert Wermes. *Pixel Detectors: From Fundamentals to Applications*. Springer, 2006.

[11] Helmuth Spieler. *Semiconductor Detector Systems*. Oxford University Press, 2006.

[12] Claude Leroy, Pier-Giorgio Rancoita. *Principles of Radiation Interaction in Matter and Detection*. World Scientific, 2009.

[13] T. Kawamoto. ATLAS: status, limitations and upgrade plans. TIPP, 2011.

[14] The FE-I4 Collaboration. *The FE-I4 Integrated Circuit Guide*, 11.6 edition, 2011.

[15] M. Barbero et al. The FE-I4 Pixel Readout Chip and the IBL Module. *Proceedings of Science*, Vertex 2011(PoS(Vertex 2011)038), 2011.

[16] M. Backhaus et al. Development of a versatile and modular test system for ATLAS hybrid pixel detctors. *Nuclear Instruments and Methods in Physics Research A*, 650:37–40, 2011.

[17] Jörn Große Knetter. *Vertex Measurement at a Hadron Collider – The ATLAS Pixel Detector*. Habilitation, Physikalisches Institut, Universität Bonn, 2008. BONN-IR-2008-04.

Danksagung

Natürlich stecken in dieser Arbeit auch viele Verdienste anderer, bei denen ich mich an dieser Stelle ganz herzlich bedanken möchte.
Prof. Dr. Arnulf Quadt danke ich dafür, dass ich in den vergangenen Monaten erstmals tiefere Einblicke in die Hochenergiephysik und die Arbeitsweise einer universitären Forschungseinrichtung gewinnen konnte.
Bei PD Dr. Jörn Große-Knetter möchte ich mich für die gute Betreuung bedanken, außerdem für die vielen Fragen, die ich stellen durfte und die geduldigen Antworten, wenn ich etwas nicht sofort verstanden habe. Es hat mir großen Spaß gemacht, die vergangenen Monate im Detektor-Team mitzuarbeiten und einen kleinen Teil zum IBL-Upgrade beitragen zu können.
Matthias und Nina möchte ich danken für das Korrekturlesen und für die kritischen und anregenden Kommentare zu meiner Arbeit.
Für die entspannte und oft auch lustige Arbeitsatmosphäre gilt mein Dank Hans und Julia. Ohne euch wäre die Arbeit im Labor sicherlich weniger leicht von der Hand gegangen.
Meine Mutter und Georg Seifert haben diese Arbeit auf die sprachlichen Aspekte hin geprüft. Vielen Dank für die Korrekturen und die hilfreichen Diskussionen über die englische Sprache.
Weiterer Dank gilt Eva, Lilly, Carla und Adrian für die Ratschläge beim Erstellen dieser Arbeit.

Erklärung nach §13(8) der Prüfungsordnung für den Bachelor-Studiengang Physik und den Master-Studiengang Physik an der Universität Göttingen:

Hiermit erkläre ich, dass ich diese Abschlussarbeit selbständig verfasst habe, keine anderen als die angegebenen Quellen und Hilfsmittel benutzt habe und alle Stellen, die wörtlich oder sinngemäß aus veröffentlichten Schriften entnommen wurden, als solche kenntlich gemacht habe.
Darüberhinaus erkläre ich, dass diese Abschlussarbeit nicht, auch nicht auszugsweise, im Rahmen einer nichtbestandenen Prüfung an dieser oder einer anderen Hochschule eingereicht wurde.

Göttingen, den 2. April 2012

(Mattia Donzelli)